Advances in Water Resources 88 (2016) 152–169

Contents lists available at ScienceDirect

Advances in Water Resources

journal homepage: www.elsevier.com/locate/advwatres

Differentiating between rain, snow, and glacier contributions to river discharge in the western Himalaya using remote-sensing data and distributed hydrological modeling

Hendrik Wulf[a,1,*], Bodo Bookhagen[a,b], Dirk Scherler[a,c,d]

[a] Department of Earth and Environmental Science, Potsdam University, Germany
[b] Department of Geography, University of California, Santa Barbara, USA
[c] Earth Surface Geochemistry, Helmholtz Centre Potsdam, GFZ German Research Center for Geosciences, Telegrafenberg, 14473 Potsdam, Germany
[d] Institute of Geological Sciences, Freie Universität Berlin, 12249 Berlin, Germany

ARTICLE INFO

Article history:
Received 15 April 2015
Revised 2 December 2015
Accepted 2 December 2015
Available online 17 December 2015

Keywords:
Runoff modeling
MODIS
TRMM
Mountain hydrology
Sutlej River

ABSTRACT

Rivers draining the southern Himalaya provide most of the water supply for the densely populated Indo-Gangetic plains. Despite the importance of water resources in light of climate change, the relative contributions of rainfall, snow and glacier melt to discharge are not well understood, due to the scarcity of ground-based data in this complex terrain. Here, we quantify discharge sources in the Sutlej Valley, western Himalaya, from 2000 to 2012 with a distributed hydrological model that is based on daily, ground-calibrated remote-sensing observation. Based on the consistently good model performance, we analyzed the spatiotemporal distribution of hydrologic components and quantified their contribution to river discharge. Our results indicate that the Sutlej River's annual discharge at the mountain front is sourced to 55% by effective rainfall (rainfall reduced by evapotranspiration), 35% by snow melt and 10% by glacier melt. In the high-elevation orogenic interior glacial runoff contributes ~30% to annual river discharge. These glacier melt contributions are especially important during years with substantially reduced rainfall and snowmelt runoff, as during 2004, to compensate for low river discharge and ensure sustained water supply and hydropower generation. In 2004, discharge of the Sutlej River totaled only half the maximum annual discharge; with 17.3% being sourced by glacier melt. Our findings underscore the importance of calibrating remote-sensing data with ground-based data to constrain hydrological models with reasonable accuracy. For instance, we found that TRMM (Tropical Rainfall Measuring Mission) product 3B42 V7 systematically overestimates rainfall in arid regions of our study area by a factor of up to 5. By quantifying the spatiotemporal distribution of water resources we provide an important assessment of the potential impact of global warming on river discharge in the western Himalaya. Given the near-global coverage of the utilized remote-sensing datasets this hydrological modeling approach can be readily transferred to other data-sparse regions.

1. Introduction

Runoff from the Himalaya is extensively used for hydropower generation, agriculture, as well as urban and rural household use in the densely populated Indo-Gangetic Plains [7,18]. In light of recent climatic change [52], glacial retreat [15,89,98], population growth [109] and groundwater depletion [86] quantitative assessment of the available water resources in this region is a crucial task [49,113]. Although discharge generated from melting of snow and ice is generally assumed to be significant, the scarcity of detailed ground-based observations make quantification of their relative contributions to Himalayan discharge difficult.

Hydrological models are useful tools to explore and quantify fluvial discharge. Runoff from melting snow and ice is commonly estimated using either surface-energy balance [4,54] or temperature-index models [59,63,83]. In the Himalayan region, large-scale surface-energy balance approaches are currently not feasible, because of poorly validated input variables (e.g., wind speed, water-vapor pressure, humidity, radiation fluxes, etc.). In contrast, temperature-index models, which represent simplified empirically based alternatives, require less input data that are usually available for most regions on Earth. However, their simplicity may lead to lower accuracy and larger uncertainties of the results [34,78,82]. Furthermore, coefficients of temperature-index models can vary significantly within individual watersheds [42,58]. For a stronger

* Corresponding author. Tel. +41 44 6355145.
E-mail address: hendrik.wulf@geo.uzh.ch (H. Wulf).
[1] Present address: Remote Sensing Laboratories, Department of Geography, University of Zurich, Zurich, Switzerland.

http://dx.doi.org/10.1016/j.advwatres.2015.12.004
0309-1708/

physical basis of the melt water generation, the shortwave radiation balances can be included in so-called *enhanced* temperature-index models [44,78,83]. Furthermore, spatially distributed models are able to account for the high-spatial variability of meteorological parameters in mountain regions [38], but require input data that approximately match the spatial resolution of the model grid.

To achieve complete input data coverage in distributed models, previous studies have commonly extrapolated low-elevation station data to higher altitudes [e.g. [20,61,95,97]]. Extrapolation of station data for catchments with a high elevation range is problematic in mountainous regions because of the high-spatial variability of both, precipitation and temperature [9,17,62]. Alternatively, several satellite systems provide processed and gridded data products that can be used for hydrological modeling [6,90]. In the Himalaya, various MODIS and TRMM data products have been successfully integrated in hydrological models by studies that focused on mean-monthly discharges [e.g., [18]], or daily discharges in very large watersheds using MODIS [e.g., [51]]. Such approaches take advantage of temporal and/or spatial averaging, which reduces the uncertainties in the remote-sensing input data that typically contain noise, artifacts, and data gaps introduced by varying surface and atmospheric conditions, as well as specific sensor characteristics and data-processing methods [28]. Therefore, hydrological models with a high spatial and temporal resolution using remote-sensing based information on water fluxes (e.g. rainfall, evaporation) or land cover (e.g. snow cover, vegetation) need to be carefully calibrated to account for these uncertainties.

Recent hydrological modeling studies indicate high snow melt contributions to river discharge in the western Himalaya on the order of 30–60% [18,51,53,95]. In contrast, estimates of glacier melt contributions to river discharge in the Himalaya vary considerably between 2% and 30%, depending mainly on differences in glacierized catchment area, precipitation, temperature, and solar radiation [2,51,53,81].

The objective of this study is to develop a distributed hydrological model that is driven by calibrated remote-sensing data to study discharges in variably-sized catchments in steep mountainous regions, where ground-based stations are rare. As part of our modeling effort, we assess to what degree calibrated remotely sensed data change the model results, when compared to simple extrapolation of station data and uncalibrated remote-sensing data. Based on the hydrological model we analyze the spatial distribution of water resources and the temporal variations of river discharge components in the Sutlej Valley for the study period from 2000 to 2012. Furthermore, we investigate the relation of glacier snow-cover periods and glacier melt. Based on our novel approach to drive a distributed hydrological model with calibrated remote sensing data, we are able to accurately quantify the spatial and temporal variations in the release of transient water storages and investigate their impact on river discharge.

2. Study area

The Sutlej River is a tributary of the Indus River and has the third largest drainage area in the Himalaya (55,000 km^2), with two-thirds being located in China (Tibet) and one third in India (Fig. 1). Starting at the mountain front, surface elevations range from 400 m to 7200 m asl. More than 80% of the catchment area is located in the semi-arid to arid orogenic interior at elevations >4000 m asl, which results in a catchment-average elevation of 4400 m asl (Supporting material – Fig. S1). Vegetation cover is thick and dense at lower elevations at the mountain front, but decreases rapidly above an elevation of 3000 m asl and is virtually absent > 3500 m asl. Therefore, the primary land cover in the Sutlej Valley is bare ground (81.7%), as compared to trees and shrubs (7.2%), cultivated areas (6.8%), glaciers (3.2%), and lakes (1.1%) [31] (Table 1). Soil cover is present only in the lower part of the Sutlej catchment, which constitutes a small fraction (< 15%) of the entire drainage area and therefore is likely to have a low impact on overall water storages.

Precipitation in the western Himalaya has pronounced seasonal and spatial variations [18]. Snowfall occurs mostly between December and March and increases with elevation and relief [50,94,110]. During the summer months, the Indian monsoon (mid July–mid September) accounts for intense rainfall, which is mostly focused along orographic barriers of the southern Himalayan front and creates a steep SW-NE rainfall gradient, with > 2 m/yr at the fontal parts to < 0.2 m/yr over a horizontal distance of < 100 km encompassing a mean elevation range of > 4000 m [17,111]. Although most monsoonal moisture is blocked by the High Himalaya, during active monsoon phases, strong convective cells sometimes migrate across this barrier and result in cloudbursts that can mobilize enormous amounts of sediments [19,25,43,111].

3. The hydrological model

3.1. Runoff production

The newly set up distributed hydrological model calculates runoff during each time step (1 day) at each cell in the gridded model space, i.e., digital elevation model (DEM), and routes the water through the river network taking flow times and runoff storage into account. Daily runoff production, RP (mm/day), at a given location is the sum of snow melt (M_s), glacier melt (M_g), and rainfall (P_r), reduced by evapotranspiration (ET), according to:

$$RP = M_s + M_g + P_r - ET \tag{1}$$

The input data for rainfall and evapotranspiration are based on calibrated remote-sensing products, and discussed in Section 4.2 and 4.3. In contrast, snow and glacier melt are computed by processing multiple remote-sensing datasets.

3.2. Snow- and glacier melt

Similar to previous studies [22,44,45,63,78,83], we use a temperature-index model that incorporates the influences of solar radiation, snow albedo, and cloud cover. Daily snow melt (mm/day) is calculated for every snow-covered cell according to:

$$M_s = \begin{cases} (T \cdot tf_s + R_{sw} \cdot srf_s) \cdot A_s, & T > T_t \\ 0, & T \le T_t \end{cases} \tag{2}$$

where T (°C) is the mean daily temperature, R_{sw} (W/m^2) is the mean daily net shortwave radiation, A_s (m^2) is the snow-covered area, tf_s (mm °C^{-1} day^{-1}) is an empirical *temperature factor* for snow melt, and srf_s (mm W^{-1} m^2 day^{-1}) is an empirical *shortwave radiation factor* for snow melt. T_t is a threshold temperature above which melt is assumed to occur (e.g., 0 °C). Glacier melt M_g (mm/day) is calculated similarly but occurs only if the corresponding cell is ice-covered and snow-free:

$$M_g = \begin{cases} (T \cdot tf_g + R_{sw} \cdot srf_g) \cdot (A_{ice} + df \cdot A_{debris}), & T > T_t \\ 0, & T \le T_t \end{cases} \tag{3}$$

where A_{ice} (m^2) is the glacier area with clean ice exposure, A_{debris} (m^2) is the glacier area with debris cover, df is a dimensionless scaling factor for reduced melt rates on debris covered ice, and tf_g (mm °C^{-1} day^{-1}) and srf_g (mm W^{-1} m^2 day^{-1}) are empirical coefficients that relate temperature and shortwave radiation, respectively, to melt water production. Because supraglacial debris cover with a thickness > 2 cm, reduces ice melt due to its shielding effect on radiation and heat fluxes [20,48,64,84], we introduce a debris factor, df, that allows reducing melt rates for debris-covered ice.

Net shortwave radiation, R_{sw}, is calculated as [78]:

$$R_{sw} = R_{sky} \cdot f_{cc} \cdot (1 - \alpha) \tag{4}$$

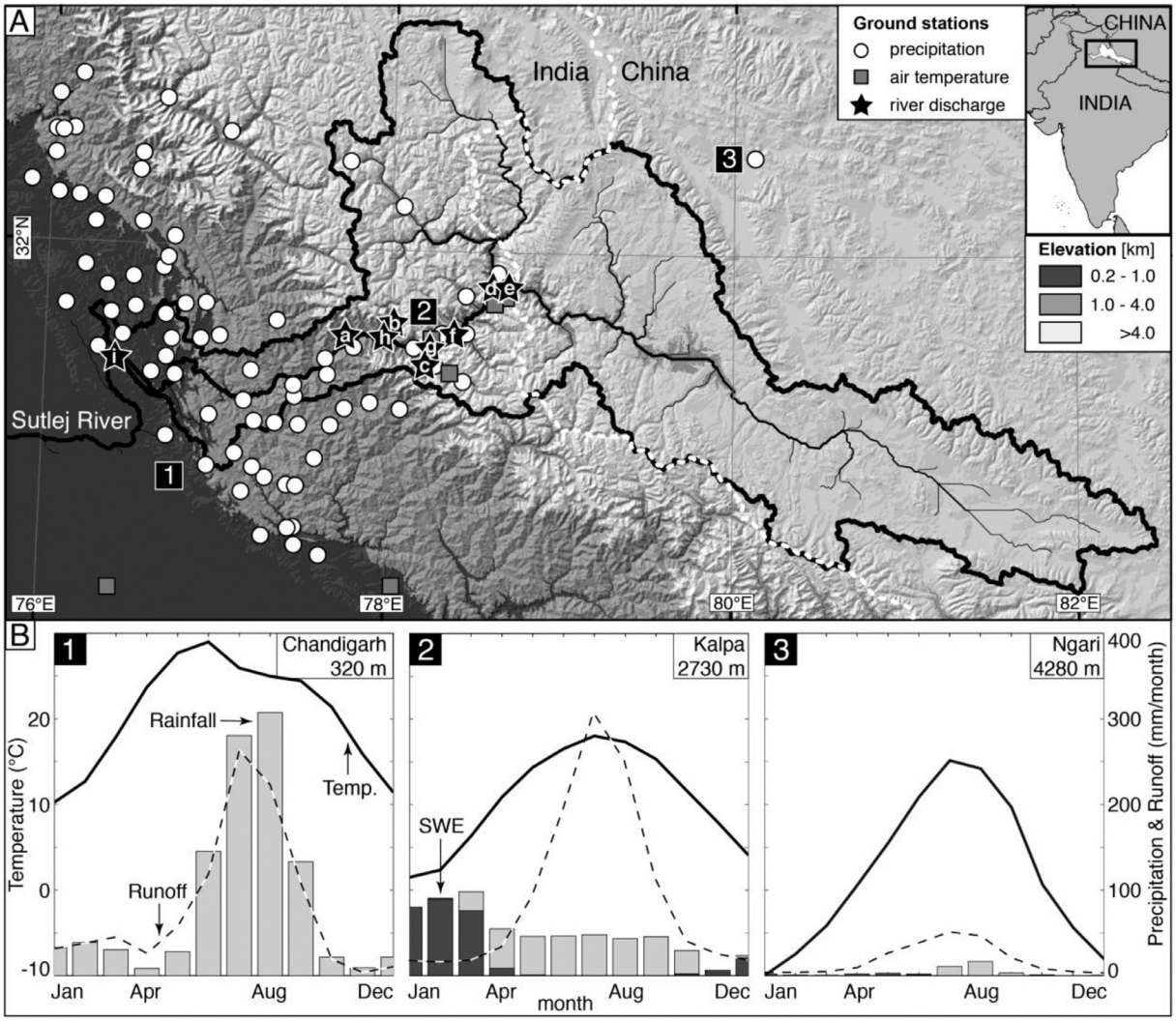

Fig. 1. (A) Shaded relief and elevation map of the western Himalaya with inset showing map location. Black polygon outlines the Sutlej catchment and defines the hydrologic model domain; white dashed line is the international border between India and China. White circles indicate weather stations recording rainfall and partially snow water equivalent. Gray squares represent weather stations in Patiala, Dehradun, Kalpa, Rakchham, Khab and Namgia (west to east), which additionally record daily minimum and maximum temperatures. Black stars denote river-gauging stations of the Sutlej main stem and tributaries at Bhakra (i), Ganvi (a), Wangtoo (h), Wanger (b), Baspa (c), Powari (g), Karoo (f), Spiti (d), Namgia (d) (west to east, cf. Table 1). (B) Characteristic ground-station data showing mean monthly temperature, precipitation, and runoff at the Himalayan Front (1), at the Himalayan Crest (2), and at the southern Tibetan Plateau (3).

where, R_{sky} (W/m^2) is the incident clear sky solar radiation, f_{cc} is a calibrated dimensionless factor, ranging between 0.61 and 1 (see Section 4.4.3), which accounts for reduction of clear sky radiation due to cloud cover, and α is the snow or ice albedo.

3.3. Runoff response

This runoff response module is based on the HBV model concept [12,13]. Similar to the hydrological modeling system PREVAH [38,104], we account for runoff storage in subsurface reservoirs by two linear storages (*SUZ* and *SLZ*; Fig. 2). We use these reservoirs to differentiate between surface runoff [*RS* (mm/day)], interflow [*RI* (mm/day)], and groundwater runoff [*RG* (mm/day)] by modeling a specific runoff response for each component (Fig. 2). The groundwater storage is further divided into fast (*RG1*) and slow-leaking (*RG2*) components. The sum of all runoff components for each time step (t) corresponds to simulated river discharge (Q_{sim}):

$$Q_{sim}(t) = RS(t) + RI(t) + RG1(t) + RG2(t) \quad (5)$$

Water flows are computed for each time step (dt), which can be defined arbitrarily. We use daily intervals based on the daily data availability of MODIS and TRMM remote sensing data and river discharge measurements. Daily runoff production (*RP*) replenishes the upper storage reservoir (*SUZ*) to generate interflow and additional surface runoff, if a certain storage threshold is exceeded [SI_{max} (mm)]. Water in the *SUZ* drains by percolation [*PERC* (mm/day)] into the lower groundwater reservoir (*SLZ*), from where groundwater runoff occurs. This hydrologic budget of both reservoirs is described by the following governing equations:

$$SUZ(t) = SUZ(t-1) + (RP(t) - (PERC(t-1) + RS(t-1) + RI(t-1))) \cdot dt \quad (6)$$

$$SLZ(t) = SLZ(t-1) + (PERC(t) - RG1(t-1) - RG2(t-1)) \cdot dt \quad (7)$$

The residence period of each runoff component (*RI, RS, RG1, RG2*) is controlled by the storage time parameters [*K0-K3* (day)]. Consequently, the generation of interflow (*RI*) and surface runoff (*RS*) depends on the content of the upper storage reservoir (*SUZ*) and the storage time parameters (*K1, K0*).

$$RI(t) = SUZ(t) \cdot (1 - e^{-\frac{t}{K1}}) \cdot dt^{-1} \quad \text{if } SUZ > 0 \quad (8)$$

Table 1
Topographic, land cover, and hydrological characteristics of the modeled catchments.

Catchments[a]		Topography							Land cover			Hydrology	
		Area	Elevation			Relief	Location		Bare ground	Vegetation	Glacier	Snow cover	Runoff
		[km^2]	Min [km]	Mean [km]	Max [km]	[km/ 5 km]	Lat [°]	Lon [°]	area [%]	area [%]	area [%]	area [%]	[m yr^{-1} m^{-2}]
Tributaries	Ganvi (a)	117	1.6	3.4	5.6	2.58	31.55	77.76	33.3	62.5	4.1	25.6	1.25
	Wanger (b)	264	2.5	4.4	5.7	2.24	31.62	78.02	69.1	16.1	14.8	55.4	1.59
	Baspa (c)	989	2.5	4.7	6.4	2.21	31.42	78.26	57.1	23.8	19.1	54.8	1.16
	Spiti (d)	12,477	2.6	5.0	6.7	1.68	31.81	78.64	92.6	1.6	5.9	38.4	0.23
Sutlej River at	Namgia (e)	30,950	2.6	4.8	7.2	0.93	31.81	78.65	91.1	7.0	1.9	19.8	0.06
	Karoo (f)	46,025	2.2	4.8	7.2	1.21	31.59	78.36	90.9	5.9	3.2	26.1	0.14
	Powari (g)	46,291	1.9	4.8	7.2	1.22	31.52	78.27	90.7	6.1	3.2	26.1	0.15
	Wangtoo (h)	48,316	1.5	4.8	7.2	1.27	31.56	77.98	89.3	7.1	3.6	26.9	0.20
	Bhakra (i)	54,926	0.4	4.4	7.2	1.30	31.41	76.43	81.7	15.1	3.2	24.1	0.23

[a] Labels in parenthesis refer to the gauging station of each catchment as indicated in Fig. 1.

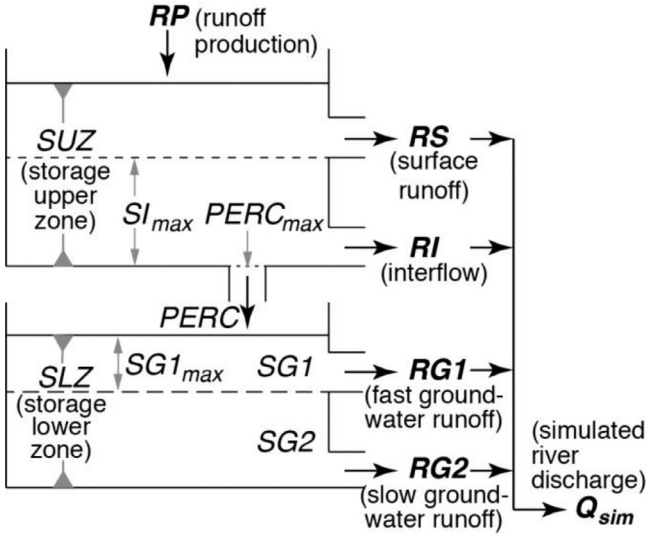

Fig. 2. Schematic overview of runoff fluxes and storage modules in the hydrological model. *SG1* and *SG2* represent fast and slow-leaking groundwater storages, respectively. SI_{max}, $SG1_{max}$, and $PERC_{max}$ represent thresholds for the generation of surface runoff, slow groundwater runoff, and the percolation rate (*PERC*), respectively.

$$RS(t) = (SUZ(t) - SI_{max}) \cdot \left(1 - e^{-\frac{t}{K0}}\right) \cdot dt^{-1} \quad \text{if } SUZ > SI_{max} \tag{9}$$

A threshold on the percolation rate [$PERC_{max}$ (mm/day)] limits the flux into the groundwater reservoir. Groundwater storage is divided into a fast-leaking storage (*SG1*) and a slow-leaking storage (*SG2*), which are filled by recharge rates [*GR1, GR2* (mm/day)] as a function of the percolation rate (PERC) [93]. The fast groundwater component [*RG1* (mm/day)] is limited by a maximal storage capacity [$SG1_{max}$ (mm)], whereas the slow groundwater component [*RG2* (mm/day)] has no upper limit. The generation of groundwater runoff is governed by the storage time parameters (*K2, K3*) and the change in storage of the groundwater reservoirs during *dt*. Constant and tunable model parameters for each catchment are listed in Table 2.

$$RG1(t) = [SG1(t-1) \cdot \left(e^{-\frac{t}{K2}}\right) + \left(1 - e^{-\frac{t}{K2}}\right) \cdot GR1(t-1) \cdot K2]/K2 \quad \text{if } SLZ > 0 \tag{10}$$

$$RG2(t) = [SG2(t-1) \cdot \left(e^{-\frac{t}{K3}}\right) + \left(1 - e^{-\frac{t}{K3}}\right) \cdot GR2(t-1) \cdot K3]/K3 \quad \text{if } SG1 > SG1_{max} \tag{11}$$

3.4. Runoff routing

To account for discharge travel times, we estimated flow velocities, v (m/s), based on a modified version of Manning's formula, according to:

$$v = sf^{-1} \cdot HR^{0.66} \cdot S^{0.5} \tag{12}$$

where, S (m/m) is the local channel gradient, HR (m) is the flow hydraulic radius and sf (dimensionless) represents a scaling factor, which is equivalent to Manning's roughness factor, to adjust the flow velocity to field observations from the Sutlej River [91] (Fig. 3). For simplicity, we assume a rectangular Sutlej River cross section and calculate hydraulic radius as a function of the river depth (D) and river width (W):

$$HR = D \cdot W \cdot (2 \cdot D + W)^{-1} \tag{13}$$

We estimate river depths and widths based on a power-law scaling with bankful discharge, Q_{bf} [e.g., [3,60]]:

$$D = x_d \cdot Q_{bf}^{y_d} \tag{14}$$

$$W = x_w \cdot Q_{bf}^{y_w} \tag{15}$$

We use the coefficients from Allen et al. [3] ($x_d = 2.71$, $y_d = 0.557$, $x_w = 0.349$ and $y_w = 0.341$), which are based on regression analysis with a dataset of 674 river cross sections across the USA and Canada. While measurements from satellite imagery to the east of our study area corroborates an exponent y_w close to ~0.4 as a general average, there exists considerable channel-width variability between contrasting lithologic and tectonic regimes that cannot currently be accounted for with a simple power-law approach [33].

For simplicity, we assume that hydraulic radii for non-bankfull discharge follow the same geometric rule as for bankfull discharge. Hence Eqs. (14) and (15) are used to calculate the hydraulic radius in Eq. (13) based on the mean annual discharge. We account for seasonally varying flow times by scaling winter flow path times according to flow velocity measurements (1.54 m/s in winter, 3.20 m/s in summer) of the Sutlej River at Luhri (31.34°N, 77.42°W) close to the mountain front at Bhakra [75] (Fig. 3). Based on these mean river discharge velocities, obtained by repeated float method measurements using a surface velocity correction factor of 0.7, the scaling factor *sf* in Eq. (12) ranges between 0.549 (winter) and 0.264 (summer). These scaling factor values are relatively high in comparison with other Manning's roughness factors, which can be attributed to the simplified assumption of a rectangular riverbed with estimated river depths at bankful discharge. To derive discharge lag times based on the average flow path velocity we calculated the euclidean distance of each cell to the catchment outlet along the flow paths by the D8 flow accumulation algorithm. Drainage networks and flow paths were extracted using the TopoToolbox v2 [92]. Finally, we delayed runoff for each pixel according to its average daily flow time from the pixel location to the drainage basin outlet (Fig. 3). This delay is measured in days (t) and sub-daily fractions (hourly delay) between day (t) and day (t+1) based on the inverse ratio of the fractions.

Table 2
Values of calibrated tunable and constant model parameters for each catchment.

Catchments		Tunable model parameter							Constant model parameter			
		srf_s [mm m^2 W^{-1} day^{-1}]	tf_s [mm °C^{-1} day^{-1}]	srf_g [mm m^2 W^{-1} day^{-1}]	tf_g [mm °C^{-1} day^{-1}]	SI_{max} [mm]	$SG1_{max}$ [mm]	$PERC_{max}$ [mm day^{-1}]	$K0$ [day]	$K1$ [day]	$K2$ [day]	$K3$ [day]
Tributaries	Ganvi	0.150	1.72	0.482	0.50	2.5	20.7	6.2	0.4	3.1	31.3	104.2
	Wanger	0.088	6.44	0.484	1.79	6.5	32.5	13.9	0.4	3.1	31.3	104.2
	Baspa	0.093	5.21	0.313	0.76	23.5	84.2	16.9	0.4	3.1	31.3	104.2
	Spiti	0.022	2.73	0.160	0.24	54.5	266.9	79.8	0.4	3.1	31.3	104.2
Sutlej River at	Namgia	0.009	0.89	0.062	1.34	35.0	183.5	29.8	0.4	3.1	31.3	104.2
	Karoo	0.021	2.54	0.138	0.28	140.1	667.1	111.1	0.4	3.1	31.3	104.2
	Powari	0.019	2.62	0.127	0.22	132.8	673.4	125.5	0.4	3.1	31.3	104.2
	Wangtoo	0.025	3.09	0.165	0.52	150.0	725.7	170.3	0.4	3.1	31.3	104.2
	Bhakra	0.019	1.80	0.119	0.38	158.7	794.8	232.0	0.4	3.1	31.3	104.2

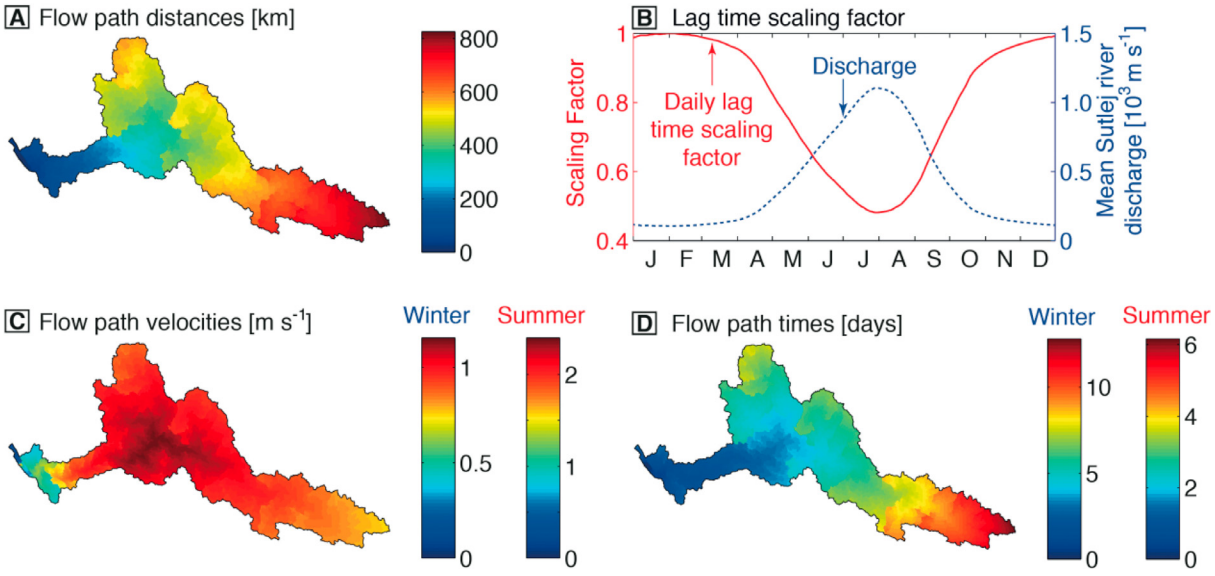

Fig. 3. (A) Flow-path distances in km for each cell to the Sutlej River at Bhakra. (B) Lag-time scaling factor based on the annual mean discharge at Bhakra smoothed with a 50-day running window. (C) Mean-seasonal flow path velocities for the path of each cell to the Sutlej River at Bahkra. Note the generally higher flow velocities in the steep sections of the middle Sutlej. (D) Mean-seasonal flow path times.

4. Model input data and calibration procedures

4.1. Ground station data

The available weather station data comprise 63 weather stations from the Indian Meteorological Department (IMD), 17 high-elevation stations operated by the Bhakra Beas Management Board (BBMB) and three weather stations that are part of the World Meteorological Organization's (WMO) Regional Basic Climatological Network (Fig. 1). The IMD stations record rainfall only, whereas the BBMB and WMO stations additionally measure snow water equivalent (SWE) by melting daily amounts of snow captured in a snow gauge. Furthermore, all WMO and four BBMB stations (Fig. 1) record daily maximum and minimum temperatures, including one automated weather station at Khab that records hourly data of rainfall, temperature, and incident solar radiation. We preprocessed the precipitation data according to quality-control measures introduced by Einfalt and Michaelides [30] and excluded unreliable values from subsequent analyses [111]. In total, the available precipitation records cover a fourteen-year time span from 1998 to 2012, but lack completeness by 52% on average. The weather stations cover a steep north–south precipitation gradient across the main Himalayan crest and range in elevation from 250 m to 4280 m asl [111] (Supporting material – Table S1). We use these precipitation records to calibrate and adjust the TRMM 3B42 rainfall data set.

In the Indian part of the Sutlej Valley, several privately owned and governmental hydropower companies operate a dense network of river-gauging stations. Most station records cover the time span from January 2004 to August 2008, although a severe flood in the Sutlej River on June 26, 2005 has led to interruptions at five stations, lasting 1–8 months [112]. The daily discharge measurements are based on stage-discharge rating curves that are annually recalculated during low-flow conditions in winter due to channel-bed changes. We use river-discharge records from five gauging stations on the Sutlej River and four of its major tributaries to calibrate and validate our model. This procedure enables us to quantify the discharge components, their uncertainties, and their spatial variation across different climatic zones in the Sutlej catchment.

4.2. Rainfall

To compute runoff due to rainfall, P_r, in our hydrological model, we tested three approaches that yield rainfall estimates with increasing spatial complexity. The first and simplest approach was to use the weather-station data and interpolate the rainfall records based on a 2D Delaunay triangulation-based interpolation method, which weights the area-of-influence associated to each weather station and performed well in previous studies with sparse data locations [79]. In our second approach we used a daily satellite-derived rainfall record, based on the TRMM product 3B42 (version 7), which has a spatial

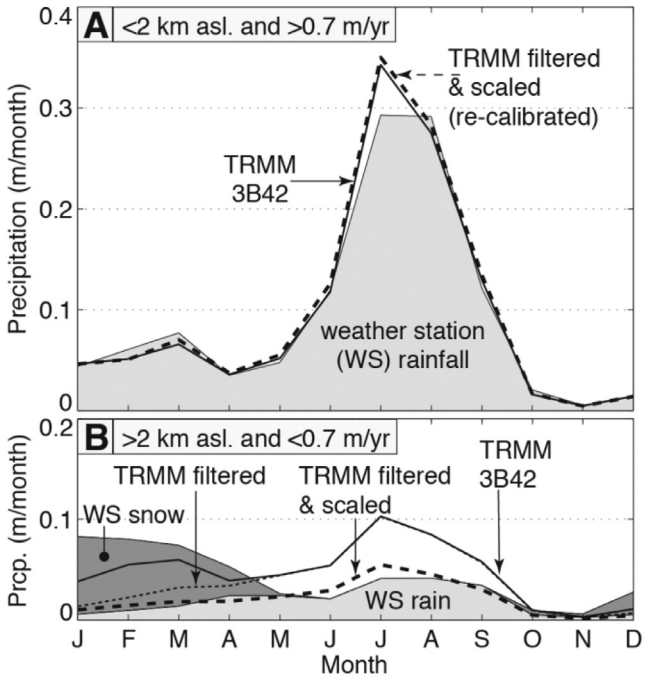

Fig. 4. (A) Comparison of original (solid line), filtered (dotted line), and filtered & scaled (re-calibrated) (dashed line) TRMM 3B42 V7 with weather station (WS) rainfall data at 66 locations below 2000 m asl for the time period 2000–2012. Scaling is based on the relation between TRMM 3B42 and weather station data (Fig. 5) and TRMM 3B42 data is filtered for snow cover and maximum daily temperatures below 0°C. Mean annual rainfall in this region is > 0.7 m/yr. (B) Comparison of original (solid line), filtered (dotted line), and filtered and scaled (re-calibrated) (dashed line) TRMM 3B42 (2000–2012) with snow water equivalent (SWE) and rainfall data of 16 weather stations (WS) located above 2000 m asl, where mean annual rainfall is < 0.7 m/yr.

resolution of 0.25° × 0.25° (~30 km × 30 km) and a temporal resolution of 3 h. This data set combines microwave and infrared rain-rate estimates from sensors onboard several low-earth orbit and one geosynchronous satellite, which are rescaled to monthly rain-gauge data [46]. Previous studies suggest that the TRMM 3B42 product is comparable to other satellite based rainfall products, which generally show a lower performance in complex terrain [e.g., [26,65,88,102]]. Although the spatial resolution of the TRMM 3B42 data makes direct comparison to weather station data difficult, Pan et al. [74] found in a comparison of different satellite-based precipitation products for the United States that rain-gauge assisted corrections of satellite products significantly enhance their skill in hydrologic predictions, especially over mountainous areas.

To assess the potential requirement for correcting the TRMM-based rainfall, we compared the TRMM 3B42 product with 84 weather-station records across our study area. In general, TRMM captures rainfall at the humid range front with mismatches < 6% during all months of the year, but overestimates rainfall by up to ~100% in the arid interior parts (Figs. 4, 5). The mismatch in the arid areas is most pronounced during the summer season (May–October). During the winter season TRMM data also indicate substantial rainfall in the high-elevation orogenic interior (Fig. 4B), despite concurrent snow coverage and temperatures below freezing. Given the coinciding increase in TRMM rainfall rates with snowfall, it appears that the TRMM data has difficulties in these areas to distinguish between snow and rainfall.

Fig. 5A shows the ratio between mean annual rainfall based on TRMM data and on weather station data for each of the weather stations, and thus by how much the TRMM data over- or under-predicts the ground measurements. Rainfall is overestimated in the arid interior part of the range by a factor of 2–5, whereas it is underestimated at the humid range front by up to 50% (Fig. 5C). These data follow a negative power-law relation with a high coefficient of determination. It is currently not clear if this is a systematic bias in the TRMM-based rain rate, an effect of the temporally sparse sampling of the satellite product or due to the high spatial variability of rainfall and associated aliasing. To further test the ability of TRMM to detect individual rainfall events, we compared daily rain rate observations by TRMM with the weather station records (Fig. 5B). In this comparison, we examine the TRMM performance based on its ability to detect (hit, *H*), not detect (miss, *M*), or erroneously predict (false alarm, *FA*) rainfall events. We only consider rainfall records above 2 mm, which represents the minimum recording level of weather stations. The false alarm rate (*FAR*) and hit rate (*HR*) are calculated according to Jolliffe and Stephenson [55] and Swets [100] by:

$$FAR = FA \cdot (H + FA)^{-1} \cdot 100 \quad (16)$$

$$HR = H \cdot (H + M)^{-1} \cdot 100 \quad (17)$$

Similar to the trend in mean annual rainfall we find a reasonably good performance (~70% hit rate, ~40% false alarm rate) of the TRMM data at the orogenic front, whereas towards the interior of the orogen, TRMM has slightly fewer hits (~60%) and a much higher false alarm rate (~70%).

In summary, our comparison revealed that the performance of the TRMM data increases with increasing rainfall amounts throughout the region, but is relatively low where rainfall is low, such as in the orogenic interior. To overcome this problem, we first filtered the satellite-based rainfall data using MODIS snow cover data (see Section 4.4.1) and air temperature data (see Section 4.4.2). TRMM rainfall events are filtered out in areas with daytime temperatures below 0 °C and are scaled in areas with snow cover by the inverse snow cover fraction. Second, we scaled the daily TRMM observations with a spatially varying factor that is based on the power-law scaling relation between mean annual rainfall derived from TRMM and the ground stations (Fig. 5A). With this third re-calibration approach, we aim to capture adequately the reduction in rainfall towards the high-elevation arid orogenic interior and to remove snow-rain confusion at higher elevations throughout the year. In the results Section 5.1, we evaluate the model performance using three different rainfall datasets: (1) the interpolated weather station data, (2) the original TRMM rainfall, and (3) the re-calibrated TRMM rainfall data.

4.3. Evapotranspiration

Evapotranspiration in our model is based on the MODIS Global Terrestrial Evapotranspiration Product (MOD16A2), which is available at ftp://ftp.ntsg.umt.edu/pub/MODIS/NTSG_Products/MOD16/MOD16A2.105_MERRAGMAO/ [69,71]. The evapotranspiration algorithm is based on a physical model using the Penman–Monteith method and considers surface-energy partitioning and environmental constraints, such as vegetation cover and meteorological conditions, on evapotranspiration [23,68,70]. The current algorithm also includes nighttime evapotranspiration and soil-heat flux among other improvements and has been evaluated across different terrain and land cover types in North America where it shows reasonable good correlation ($r^2 = 0.81$) with ground-based data [69].

The gridded evapotranspiration data are 8-day composites with a spatial resolution of 1 km. After resampling the data to the spatial resolution of the model domain, we disaggregated the 8-day composite to daily data by linear interpolation between two 8-day composites. Because there are no developed soils and associated vegetation covers in more than 85% surface area of the Sutlej catchment, we assume near-surface soil water storage is negligible. Therefore we consider only evaporation from the surface layer during days with rainfall. The resulting effective precipitation (rainfall reduced by evapotranspiration) represents the daily budget of rainfall and evapotranspiration within a modeling cell. If daily evapotranspiration

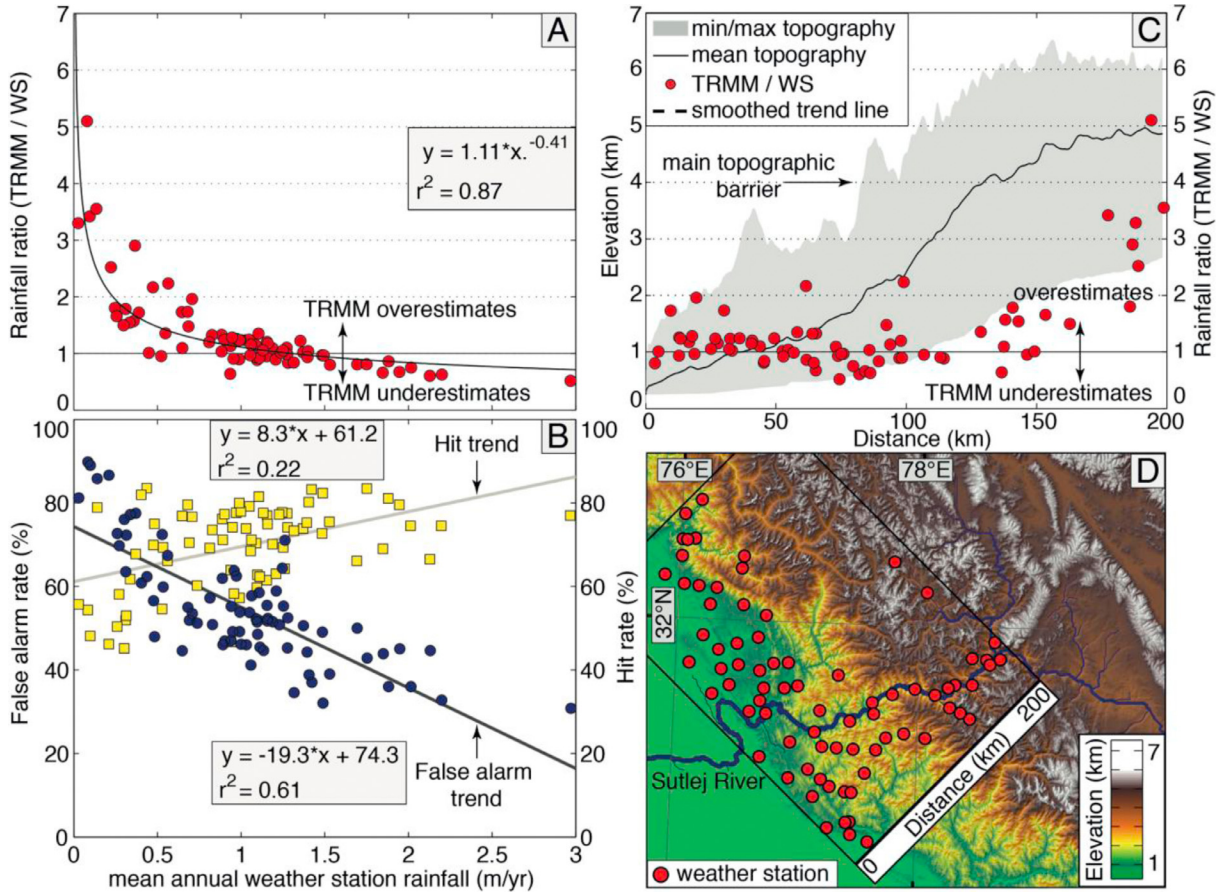

Fig. 5. (A) Correlation of mean annual weather station (WS) rainfall data versus the ratio of mean annual TRMM 3B42 to WS data for the period 2000–2012. This rainfall ratio indicates a scaling factor by which TRMM over (>1) or underestimates (<1) weather station records. (B) Analysis of TRMM 3B42 data regarding its probability of detection and misinterpretation of daily rainfall at weather stations. (C) Topographic swath profile of the western Himalaya and the mean annual precipitation ratio of TRMM 3B42 and WS records. (D) Location of weather stations and the topographic swath profile.

exceeds rainfall, the effective rainfall is set to zero. The effective precipitation has an average annual evapotranspiration fraction of 0.21, which agrees reasonably well with field-based data from the Central Himalaya, where ~15% of the daily moisture supply is recycled by evapotranspiration [8].

4.4. Snow and ice melt components

4.4.1. Fractional snow cover (FSC)

Snow melt in our model occurs when a given pixel is snow covered and temperatures are above zero. However, we excluded lake areas from our snowmelt module, because snowmelt on frozen lakes does not infiltrate into the ground, as it gradually turns into lake water with a considerable time delay. In our model we used daily fractional snow cover (FSC) observations that are derived from the MODIS instrument onboard the Terra and Aqua satellites of the NASA Earth Observation System. The globally available MOD10A1 (Terra) and MYD10A1 (Aqua) products (current version 5) provide daily observations of FSC and snow albedo, with a spatial resolution of 500 m [40]. Terra images are available since March 2000 and Aqua images since July 2002. The MODIS snow detection algorithm employs the normalized difference snow index (NDSI), which determines the difference in reflectance of snow between visible and short infrared wavelengths [40,41]. FSC gives the fraction of a pixel, which is snow covered, and is computed from a functional relationship between MODIS NDSI and higher resolution Landsat FSC data [87]. Comparison of MODIS snow products with ground measurements in the western US and Austria have yielded accuracies of 94–95% [57,76]. However, it should be noted that characterizing snow cover by spectral mixing is more accurate than empirical methods based on the NDSI, especially during periods of accumulation and melt [85].

The utility of the MODIS snow-cover products for hydrological modeling is limited by cloud cover, which causes data gaps. We reduced these data gaps by first complementing missing Terra data with Aqua snow-cover observations from the same day [28,37]. As a result, the average data gaps in Terra FSC imagery reduce from 37.4 ± 27.8% to 31.9 ± 26.5%. In a next step, we corrected for artifacts introduced by large viewing angles and other systematic errors with spline interpolation on the FSC time series. The smoothing splines are weighted based on the sensor zenith angle, which is provided in the MODIS surface reflectance product MOD09GA [28]. Finally, we filled the remaining data gaps, with average durations of 2.1 days, by piecewise linear interpolation [36].

Besides cloud-cover gaps, the daily MODIS snow-cover product is also affected by snow/cloud discrimination errors [28,39]. Despite improvements in the cloud detection algorithm in the recent version (v5), the MODIS snow-cover algorithm occasionally confuses cloud with snow cover. These problems are associated with cloud-shadowed land and cloud type identification errors [39]. It is important to filter out these confusions, as they are typically associated with low elevations and high temperatures, which can cause considerable snow-melt runoff. To filter erroneous snow cover we calculated the daily average snowmelt elevation and excluded all snow cover that is 2000 m below this reference.

Based on this snowmelt elevation filter, we analyze the temporal distribution of clouds misclassified as snow for the combined

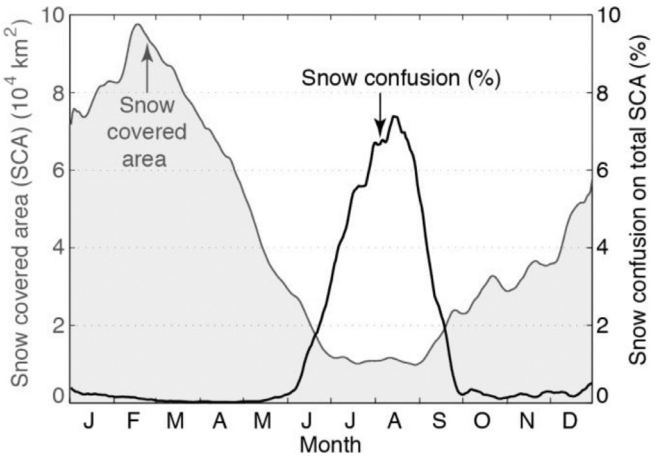

Fig. 6. Mean annual (2000–2012) distribution of snow covered area (SCA) and the percentage of misclassified snow on total snow cover (M*D10A1). We applied a 10-day moving average filter for enhanced visibility.

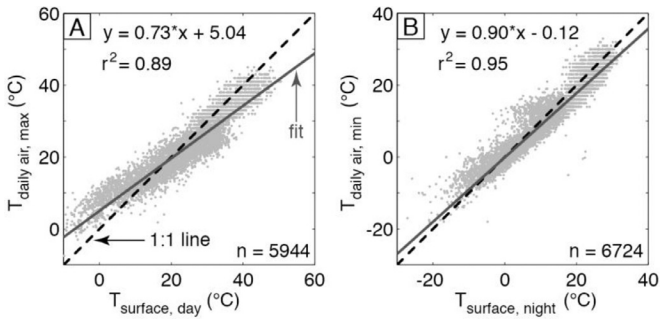

Fig. 7. (A) Linear regression of daily maximum air temperatures from Kalpa, Rakchham, Namgia, Patiala, and Dehradun (cf. Fig. 1) versus daytime MODIS Terra land surface temperatures (LST) weighted by the satellite sensor angle. In general, data with high residuals have higher sensor angles. (B) Same regression as in A for daily minimum temperatures versus nighttime MODIS Terra LST. Regressions for the MODIS Aqua sensor display the same trend (Fig. S3). Nighttime correlation includes more data points as cloud cover at night is generally lower.

Aqua and Terra FSC observations (Fig. 6). Here, we find pronounced snow/cloud confusions during the monsoon season, when the Himalayan front is affected by a dense monsoonal could cover and annual snow cover is at its minimum. Because these snow misclassifications are often associated with high summer temperatures, they increase annual snowmelt in Sutlej Valley by about 1.8%.

4.4.2. Temperature

We tested three different strategies to compute air temperatures and evaluated the accuracy of each approach by comparing generated temperatures with weather-station records to use the most favorable approach in our hydrological model. The simplest chosen approach is based on the extrapolation of weather station air temperatures from Kalpa (Fig. 1) using a constant atmospheric lapse rate of −6.5 °C/km [11]. The second approach incorporates temperature data from five weather stations to calculate a seasonally varying atmospheric lapse rate. We use daily minimum and maximum temperatures from weather stations in Patiala (250 m), Dehradun (680 m), Kalpa (2730 m), Rakchham (3130 m), and Namgia (2840 m) to calculate the daily day and nighttime air temperature lapse rate (cf. Fig. 1). Depending on seasonal variations in the atmospheric moisture content we observe a high lapse rate during winter and a low lapse rate during summer (Fig. S2) [29]. Accentuating the seasonal lapse-rate trend we calculate a mean daily lapse rate for the day and nighttime, which we use to extrapolate minimum and maximum air temperatures measured in Kalpa. The mean annual lapse rate is −5.2 ± 1.6 °C/km and −5.7 ± 1.0 °C/km for day- and nighttime, respectively.

The third approach is based on the MODIS land surface temperature (LST) product (MOD11A1 and MYD11A1) [108], which we calibrated with local weather station data to derive a distributed daily air temperature dataset. The MODIS-derived LST data are based on the view-angle dependent split-window LST algorithm, which corrects for atmospheric and emissivity effects in the thermal infrared signal over various land cover types [107]. Refinements in the algorithm of the latest LST version 5 improved the accuracy and stability of LST data especially in high-altitude regions [106]. Most validation studies indicate that the accuracy of MODIS LST data is better than 1 K [24,106,108]. However, the precise retrieval of snow-surface temperatures is difficult, because snow emissivity varies with the sensor viewing angle [27]. In addition, mixed pixels, which show exposed land and snow cover within the 1 × 1 km MODIS LST area, are likely to further complicate the snow temperature retrieval.

Temperature-index models for estimating snow and ice melting are usually run with above-ground air temperatures, which reflect both, incoming longwave atmospheric radiation and sensible heat flux, and thereby more than three-quarters of the entire energy source for melting [73]. The difference between surface and air temperatures is mainly controlled by the surface energy balance [80]. Therefore, shortwave radiation fluxes (e.g., solar radiation), strongly affect daytime surface temperatures, whereas their impact on nighttime temperatures is minor. The correlation of MODIS day- and nighttime LST with daily maximum and minimum air temperatures of five weather stations in our study area illustrates these differences (Fig. 7). Based on these relations, we calculated the corresponding air temperature of Aqua and Terra LST observation.

Similar to the snow cover data, the LST data are affected by data gaps due to cloud cover and by other distortions due to steep sensor viewing angles. We reduced these data gaps at first by combining successive Terra and Aqua observations from the same day and the same night. As a result, the average data gaps during the daytime (Terra: 39.7 ± 27.6% (mean ± 1 sigma standard deviation); Aqua 47.3 ± 26.9%) and nighttime (Terra: 30.3 ± 23.1%; Aqua 28.9 ± 21.9%) observations reduce to 33.6 ± 26.9% and 21.7 ± 21.4%, respectively. In a next step, we replaced missing data based on linear regressions between scaled MODIS temperature time series of each pixel and the air temperature record of the weather station in Kalpa (see Fig. 1), weighted by the sensor viewing angles. In addition, we used the associated *quality check* datasets (QC_day and QC_night) of the MOD11A1 product to reduce regression weights by half for MODIS LST data flagged with “other quality”. Finally, we corrected for artifacts in the scaled MODIS temperatures introduced by large viewing angles and other systematic errors with weighted spline interpolation in analogy to the final snow cover processing procedure.

The correlation of air temperatures derived by our three approaches with air temperature records from weather stations at Rakchham, Namgia, Patiala, and Dehradun (cf. Fig. 1) shows that scaled MODIS day and nighttime temperatures yield the best results (Table 3, Fig. S4). Therefore, we use our third approach based on MODIS data to calculate air temperatures that drive snow and glacier melt.

4.4.3. Incoming shortwave radiation

The incoming shortwave radiation (clear sky radiation) is calculated using standard GIS procedures that account for direct and diffusive components [16]. All parameters of the radiation module are given in Table S2. We computed daily averages of quarter-hourly free sky incoming solar radiation for each specific model cell location, based on a digital elevation model derived from the Shuttle Radar Topography Mission (version 2) [32], where voids have been patched with data from topographic maps (J. de Ferranti, 3″ resolution digital

Table 3
Evaluation of air temperature datasets based on linear regressions with weather-station records.

Approach	Method	Regression parameter					
		r^2		*rmse* [°C]		*Fit slope*	
[#]		Day	Night	Day	Night	Day	Night
1	Seasonally constant lapse rate (−6.5 °C/km)	0.84	0.90	3.72	3.10	0.83	0.94
2	Seasonally variable day- and night lapse rate	0.89	0.92	2.95	2.51	0.90	0.90
3	Scaled MODIS LST data	0.91	0.94	2.80	2.45	1.02	0.99

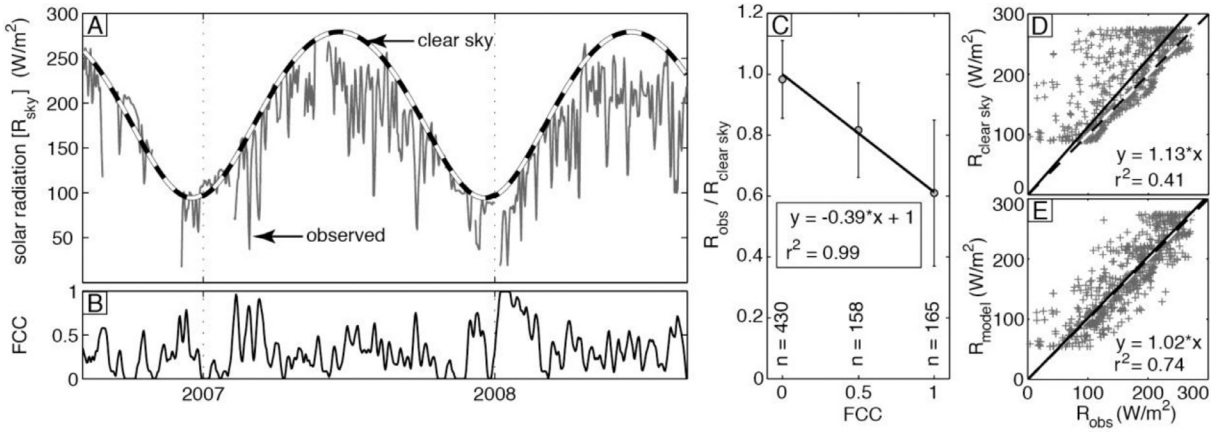

Fig. 8. (A) Comparison of mean daily observed (R_{obs}) and computed ($R_{clear\ sky}$) incoming solar radiation from August 2006 to August 2008 at Khab (cf. Fig. 1). (B) Fractional cloud cover (FCC) is derived from MODIS Aqua and Terra daytime measurements. For enhanced visibility, we smoothed FCC and R_{obs} by a 5-day running average window. (C) Correlation of R_{obs} and $R_{clear\ sky}$ versus fractional cloud cover. The linear fit is weighted by the occurrences (n) of cloud cover fractions and fixed to the origin ($x = 0, y = 1$). (D) Scatter plot of R_{obs} and $R_{clear\ sky}$. (E) Scatter plot of R_{obs} and corrected modeled solar radiation (R_{model}), which is based on $R_{clear\ sky}$ and FCC.

elevation data for Asia, 2007, http://www.viewfinderpanoramas.org/dem3.html).

Clouds reflect and absorb incoming solar radiation [99] and therefore reduce snow and glacier melt [77]. We estimate this reduction in our study area by comparing observed solar radiation, measured at Khab (Fig. 1), with the computed clear sky radiation and the daily cloud cover (Fig. 8).

We derived a daily fractional cloud cover (FCC) for each pixel by averaging the cloud-flags (0 for cloud-free and 1 for cloud-covered) from the FSC products by the Aqua and Terra satellites. These two daily MODIS observations are acquired during late morning (mean solar time: 10:51 ± 0:31 h) by Terra and early afternoon (mean solar time: 13:13 ± 0:30 h) by Aqua. We used the relation stated in Fig. 8C to account for reduction in incoming solar radiation due to cloud cover and calculated the mean daily net shortwave radiation according to Eq. (4) (see Section 3.1). The snow albedo used in Eq. (4) is part of the MODIS snow-cover product, which we processed by the same methodology as described for the snow cover product (see Section 4.4.1). For glacial surface areas we used a constant surface albedo of 0.34 for debris-free ice and 0.15 for debris-covered ice [21].

4.4.4. Glacial cover

We used the Randolph Glacier Inventory provided by the Global Land Ice Measurements from Space Initiative (GLIMS) available at http://www.glims.org/RGI/, which was recently updated based on the study by Frey et al. [35] to provide a comprehensive glacier inventory of the western Himalaya (GLIMS, and NSIDC, 2012). The data provided by Frey et al., [35] are based on classification of Landsat ETM+ Band 3/5 ratio images from September 2001 and Palsar coherence images to distinguish between debris-free and debris-covered glacial parts. We neglect changes in glacial coverage during our study period, because these are small compared to the 500-m spatial resolution of our model [89]. Based on the high-spatial resolution (30 m) of the ice-cover data we generated fractional debris-free and debris-covered ice areas for each model cell that contains ice (Fig. 9). The total glaciated area within the Sutlej catchment accumulates to 1761 km^2 that corresponds to 3.2% of which ~8% are debris-covered.

4.5. Model application and calibration

Based on our enhanced distributed hydrological model and the remotely sensed input data we simulated river discharge at nine locations (stars in Fig. 1) covering various spatial scales and climatic environments (Table 1). We calculate daily runoff from April 2000 to December 2012 at each cell in the gridded model space (463 m) of the Universal Transverse Mercator (UTM) projection 44N.

Previously, we introduced a set of tunable and constant parameters, which drive the hydrological model (Table 4). To calibrate the snow- and glacier melt, we use four adjustable parameters (srf_s, tf_s, srf_g, tf_g). In our runoff response approach, we use the minimum of three more adjustable parameters (SI_{max}, $SG1_{max}$, $PERC_{max}$) to avoid complex parameter interaction (Table 4). Furthermore, the runoff response module includes four constants (*K0, K1, K2, K3*), which were adopted from default values of the PREVAH hydromodel [103]. Additional constant parameters of the snow and melt module include the threshold temperature (T_t) of 0 °C and the debris factor (*df*) of 0.7 to account for reductions in glacier melt due to thick debris cover. This debris factor is derived from annual surface mass-balance measurements (2002–2010) of debris-covered and debris-free parts on the Chhota Shigri glacier in the neighboring Chandra river basin [5], which we consider to be representative for a generally thick and widespread debris cover in the western Himalaya [89].

We define the range of parameter values in the snow- and glacier melt module based on their contribution to river discharge. The lower and upper bound of each glacier melt factor can contribute 0–50% to observed river discharge, respectively. Likewise, the lower and upper

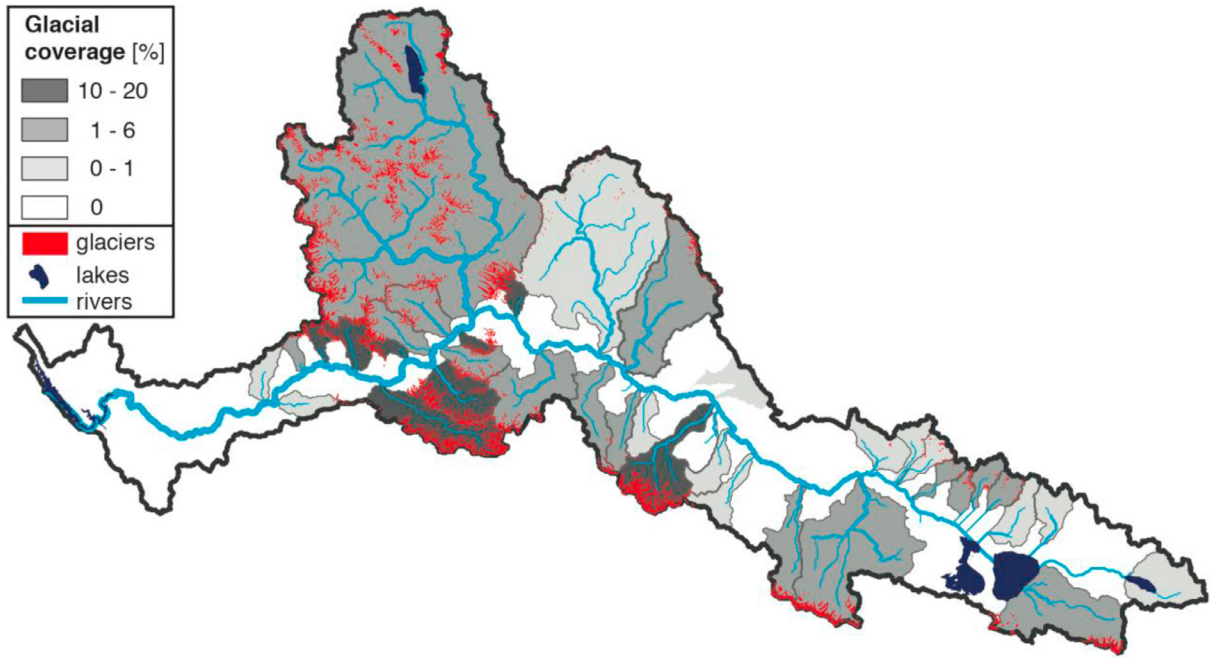

Fig. 9. Glacial coverage for Sutlej tributary basins > 100 km^2 overlain by glacial extent, lakes, and rivers. Ice-coverage is based on Frey et al., [35]

Table 4
Tunable and constant parameters of the melt and runoff response routine.

Parameter	Description	Unit	Range[a]	Value[a]	Estimation method
Snow and glacier routine					
srf_s	shortwave radiation factor for snow melt	[mm W^{-1} m^2 day^{-1}]	0–0.129	0.019	Calibration
tf_s	empirical temperature factor for snow melt	[mm °C^{-1} day^{-1}]	0–7.75	1.80	Calibration
srf_g	shortwave radiation factor for glacial melt	[mm W^{-1} m^2 day^{-1}]	0–0.645	0.119	Calibration
tf_g	empirical temperature factor for glacial melt	[mm °C^{-1} day^{-1}]	0–32.28	0.38	Calibration
df	Scaling factor for debris-covered ice	[dimensionless]	–	0.7	[5] [b]
T_t	Threshold temperature	[°C]	–	0	[103] [c]
Runoff response routine					
SI_{max}	Threshold content of the lower SUZ for generation of surface runoff (SGR)	[mm]	0–1000	158.7	Calibration
$SG1_{max}$	Threshold content of the SG1 for generation of slow-leaking recharge	[mm]	0–1000	794.8	Calibration
$PERC_{max}$	Maximal deep percolation rate	[mm day^{-1}]	0–1000	232.0	Calibration
$K0$	Storage time for surface runoff	[day]	–	0.42	[103][c]
$K1$	Storage time for interflow	[day]	–	3.13	[103][c]
$K2$	Storage time for quick groundwater flow	[day]	–	31.25	[103][c]
$K3$	Storage time for slow groundwater flow	[day]	–	104.16	[103][c]

[a] Range and value of tunable parameters are given exemplarily for the Sutlej catchment at Bhakra.
[b] value is based on mass balance data published by Azam et al., [5].
[c] use of PREVAH-default values for the respective runoff type storage time as defined in Viviroli et al. [103].

bound of each snow-melt factor can contribute 0–90% to observed river discharge, respectively.

To calibrate the tunable parameters (tf_s, tf_g, srf_s, srf_g, SI_{max}, $SG1_{max}$, $PREC_{max}$), we used an automatic optimization method that finds the best model performance based on the Nash-Sutcliffe efficiency (NSE) [72] and the relative volume error (RVE) between simulated (Q_{sim}) and observed discharges (Q_{obs}) [1]:

$$NSE = 1 - \frac{\sum_{i=1}^{N}[Q_{sim}(i) - Q_{obs}(i)]^2}{\sum_{i=1}^{N}[Q_{obs}(i) - \bar{Q}_{obs}]^2} \tag{18}$$

$$RVE = 100 \cdot \frac{\sum_{i=1}^{N}[Q_{sim}(i) - Q_{obs}(i)]}{\sum_{i=1}^{N} Q_{obs}(i)} \tag{19}$$

where i is the time step, N is the total number of time steps, $\bar{Q}_{obs}$ is the mean of Q_{obs} over the calibration/validation period. For a favorable model performance (p), the NSE should be close to the maximum value of 1 and the RVE value should be close to zero.

$$p = \frac{NSE}{1 + |RVE|/100} \tag{20}$$

This constrained nonlinear optimization method finds the minimum (best performance) of a scalar function with several variables for a given initial estimate. By generating 100 random starting points for each of our seven tunable variables within their lower and upper limits we exclude local minima to confidently detect the best performance parameters for the global function minimum.

For each gauging station we divided the river discharge dataset in two halves, using the first data period to calibrate the model and the second period to validate its performance (Fig. 10). The calibrated and constant model parameters that drive the snow- and glacier melt-module and the runoff response module are given in Table 2.

We tested the model sensitivity to variations (10% incremental steps) of each calibration factor for snow and glacier melt around their optimal values on model performance (Fig. 11). The model sensitivity of single melt factors depends on the contribution of the

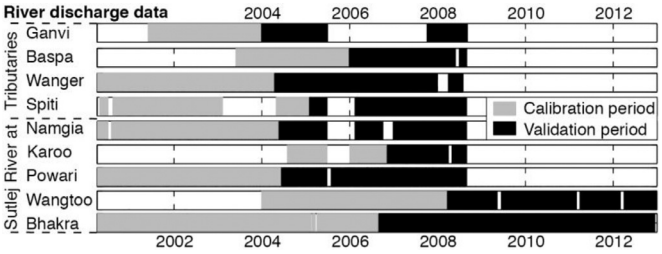

Fig. 10. Overview of observed river discharge data at gauging stations of the Sutlej River and its tributaries (cf. Fig. 1). We calibrate the hydrological model using the first data period (gray) and validated its performance based on the second data period (black).

respective melt component to total river discharge, which varies among the river catchments. In general, the hydrological model is more sensitive to variations in snow-melt factors as compared to glacier-melt factors. Therefore, we conclude that variations in the reduction of glacier melt below debris cover (factor 0.7 in this model) will have a low impact on the model performance.

5. Results

5.1. Simulated river discharge

First, we evaluate the model performance of the different rainfall datasets that are based on (1) weather station data, (2) original TRMM 3B42 data, and (3) re-calibrated TRMM data (see Section 4.2). Both, the original TRMM 3B42 data and the interpolated weather station dataset result in excessive rainfall runoff, which exceeds observed river discharge by more than two orders of magnitude (Table 2) in the high-elevation arid regions of the southern Tibetan Plateau (i.e., Spiti and Sutlej at Namgia catchments, cf. Fig. 1). Excess rainfall in the interpolated weather station dataset is due to the lack of weather station data in the high-elevation arid regions. Therefore, rainfall events recorded at distant weather stations in semi-arid regions are wrongly extrapolated to high-elevation arid regions. Similarly, missing weather station data from the orogenic interior may affect the original TRMM 3B42 dataset, as rainfall magnitudes cannot be rescaled to monthly rain-gauge data. Accordingly, the original TRMM 3B42 data does not adequately represent the decrease in rainfall across the Himalaya. We observe the best model performance using the re-calibrated TRMM rainfall dataset, which also results in a realistic partitioning of discharge sources (Table 5).

Using the re-calibrated TRMM data, simulated river discharges capture very well the observed discharges (Fig. 12). However, high-elevation catchments with relatively large rainfall contributions, such as Ganvi and the Sutlej catchment upstream of Namgia, are not adequately represented as snowfall-dominated catchments. Apart from these two catchments, the remaining watersheds yield high performance measures with NSE values ranking between 0.68 and 0.78 and show a high degree of consistency among each other (Table 5).

Our modeling results covering the period April 2000 to December 2012 indicate that annual average Sutlej River discharge (Sutlej at Bhakra) is sourced approximately half by effective rainfall ($55 \pm 5.1\%$) and half by snow ($35 \pm 5.1\%$) and glacier melt ($10 \pm 3.4\%$) (Table 5). Along its course from high to low elevations the contribution of glacier melt to Sutlej River discharge decreases from about 30% to 10%. Rainfall dominates river discharge in catchments at the Himalayan front, whereas snow melt dominates river discharge in the high elevation southern Tibetan Plateau and the main Himalayan crest.

5.2. Spatiotemporal distribution of hydrologic components

In general, mean annual runoff within the Sutlej Basin is characterized by major regional differences (Fig. 13A). The southern Tibetan Plateau is characterized by low precipitation and runoff due to its low relief and its location leeward of the main orographic barrier. The high-relief region of the main Himalayan crest captures most winter snowfall, which is also reflected by large numbers of glaciers (Fig. 9). The resulting increases in snow and glacier melt come along with moderate increases in monsoonal rainfall causing total river discharge to rise by up to one order of magnitude. This region of pronounced snow and glacier melt coincides with the steepest section of the Sutlej River profile where topographic relief is highest (Figs. 13A, 14B). In contrast, the Himalayan front is dominated by rainfall due to lower surface elevations and its windward location along the main orographic barrier. Increasing vegetation cover and temperatures cause high evapotranspiration rates (ca. 0.4 m/yr) while snow and glacier melt decrease from ca. 60% to 0% in this area.

The cumulative runoff of each Sutlej River tributary (>100 km^2) shows that the Spiti and Baspa River are the major contributors of the Sutlej River (Fig. 13B). Analysis of the relative contributions to Sutlej River discharge in the downstream direction reveals that snowmelt is the dominant runoff source in most of the high-altitude part of the catchment and down to a river elevation of ~590 m. Downstream of this point, which corresponds to a linear distance of about 40 km from the mountain front, effective rainfall becomes the dominant discharge component (Fig. 13C).

We estimated the spatial distribution of snow melt for the period October 1st, 2001 to September 30th, 2012 by the "inverse melt"

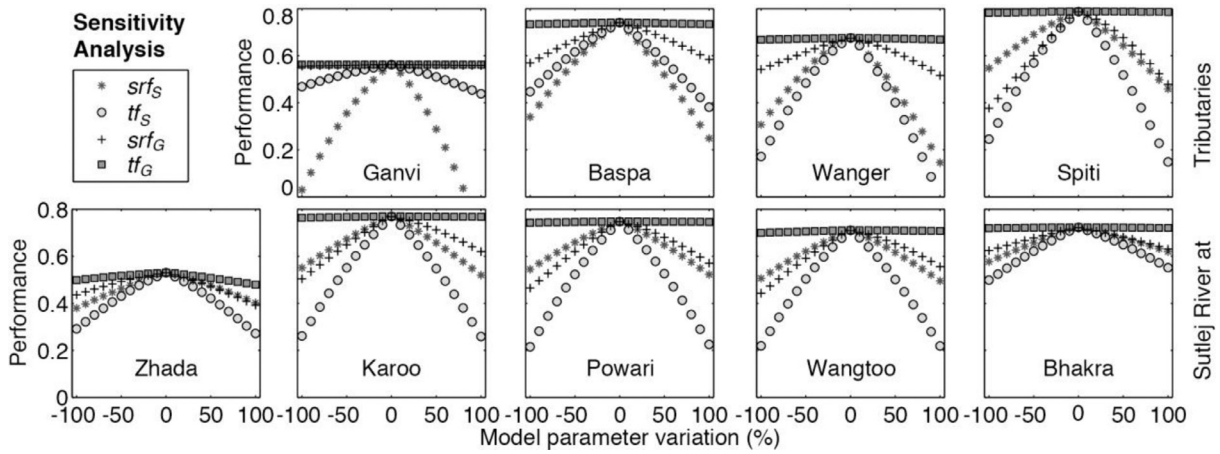

Fig. 11. Sensitivity analysis of the shortwave radiation factors for snow- (srf_s) and glacier melt (srf_g) and the thermal factors for snow- (tf_s) and glacier melt (tf_g).

Table 5
Comparison of our three different rainfall dataset by their Nash Sutcliffe Efficiency (NSE), relative volume error (RVE), and their mean annual catchment rainfall (Rain).

Rainfall datasets:		(1) Weather station data			(2) TRMM original			(3) TRMM re-calibrated			(3) Discharge sources[a]		
Catchments		NSE [Dimensionless]	RVE [%]	Rain [mm/yr]	NSE [Dimensionless]	RVE [%]	Rain [mm/yr]	NSE [Dimensionless]	RVE [%]	Rain [mm/yr]	Snow [%]	Ice [%]	Rain-ET [%]
Tributaries	Ganvi (a)	0.50	−5.9	494	0.27	21.8	745	0.59	1.4	511	58	1	41
	Wanger (b)	0.55	−2.6	245	0.54	12.3	478	0.68	−2.3	162	72	15	13
	Baspa (c)	0.77	9.3	266	0.56	15.6	514	0.75	−6.5	218	75	13	13
	Spiti (d)	−7.49	123.6	273	−0.16	39.0	152	0.78	−0.2	31	67	22	11
Sutlej River at	Namgia (e)	−107.91	531.8	392	−36.81	309.9	237	0.54	−1.6	50	42	19	39
	Karoo (f)	−6.30	135.4	351	−2.90	100.2	213	0.71	2.8	44	65	18	17
	Powari (g)	−18.22	194.2	350	−3.17	98.9	213	0.75	−2.2	45	66	17	18
	Wangtoo (h)	−2.60	99.7	348	−3.16	84.1	218	0.72	−3.2	51	66	18	16
	Bhakra (i)	−5.24	96.1	392	−1.99	68.4	300	0.72	1.1	131	35	10	55

[a] The discharge sources represent the modeling results for the third re-calibrated TRMM rainfall dataset, which we used to drive the hydrological model.

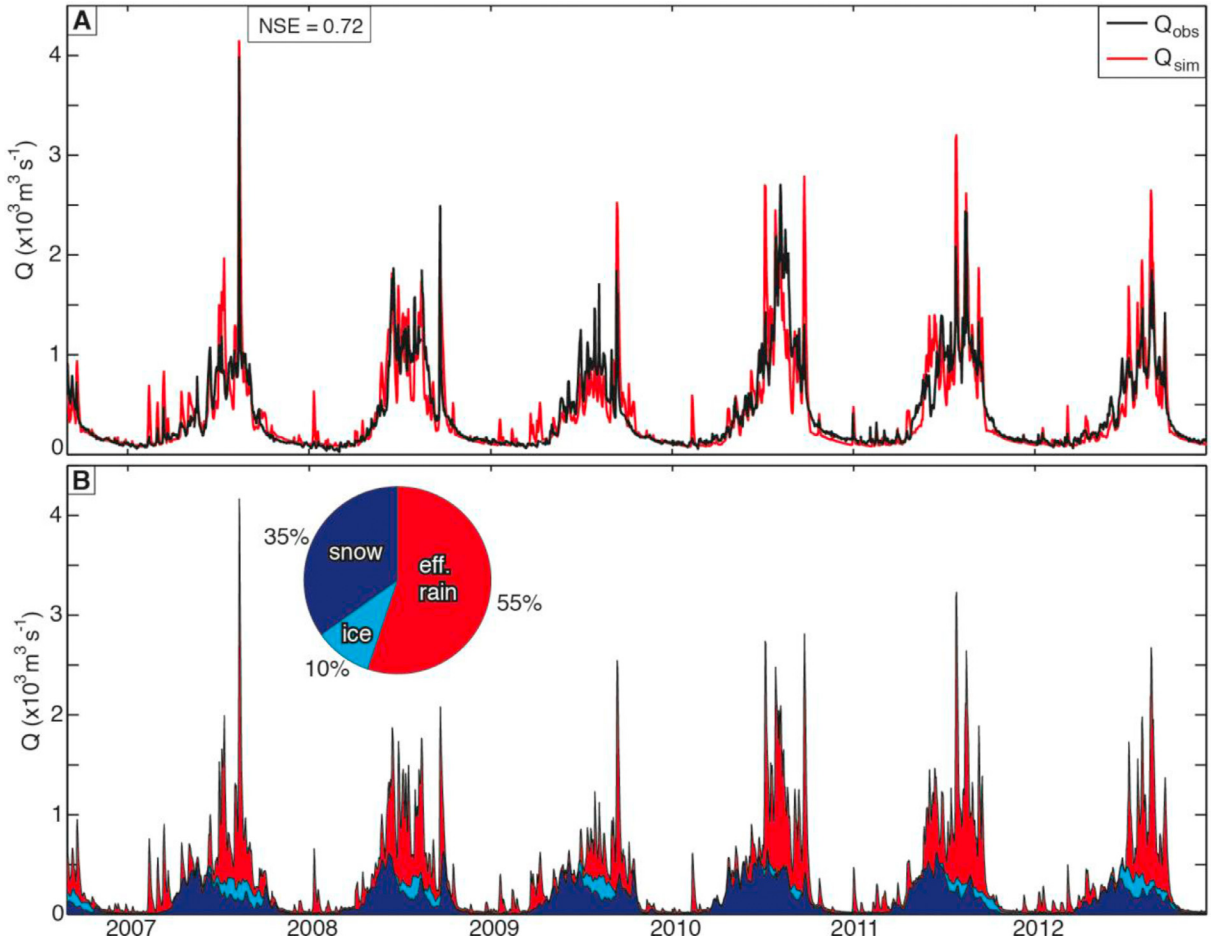

Fig. 12. (A) Comparison of the observed and simulated daily discharges of the Sutlej River at Bhakra near the mountain front (cf. Fig. 1) from September 2006 to December 2012. (B) Sum of the single simulated discharge components illustrating the different stacked contributions to total runoff. Pie chart represents the contribution of each runoff component to total discharge over the 6-year period.

approach [67] (Fig. 14A). This annual summation of daily snow melt represents all the snow that melted during the hydrological year (October–September). Although snow can persist throughout the melt season at high elevations, snow accumulation areas are mainly restricted to glacial accumulation zones. Therefore, we assume that our snow-melt summation is roughly equal to annual amounts of snow water equivalent.

The snow-melt distribution varies across the western Himalaya with snow melt starting at surface elevations of about 1800 m asl that increases northeastward along with increases in elevation and relief (Fig. 14B). Snow melt is high (> 0.5 m) in the region of the main Himalayan crest, from where it decreases towards the Tibetan Plateau. Despite high elevations, this decline is mainly due to an increasing leeward distance from the main orographic barrier and a decrease in topographic relief that effectively captures orographic precipitation (Fig. 14B). Accordingly, we find large spatial variations in glacier melt between glaciers situated in the Himalayan crest region and glaciers bordering the Tibetan Plateau (Fig. S5). Whereas low average ablation rates are typical for large ice fields in the Himalayan crest region, generally high ablation rates characterize multiple small glaciers at the southern Tibetan Plateau.

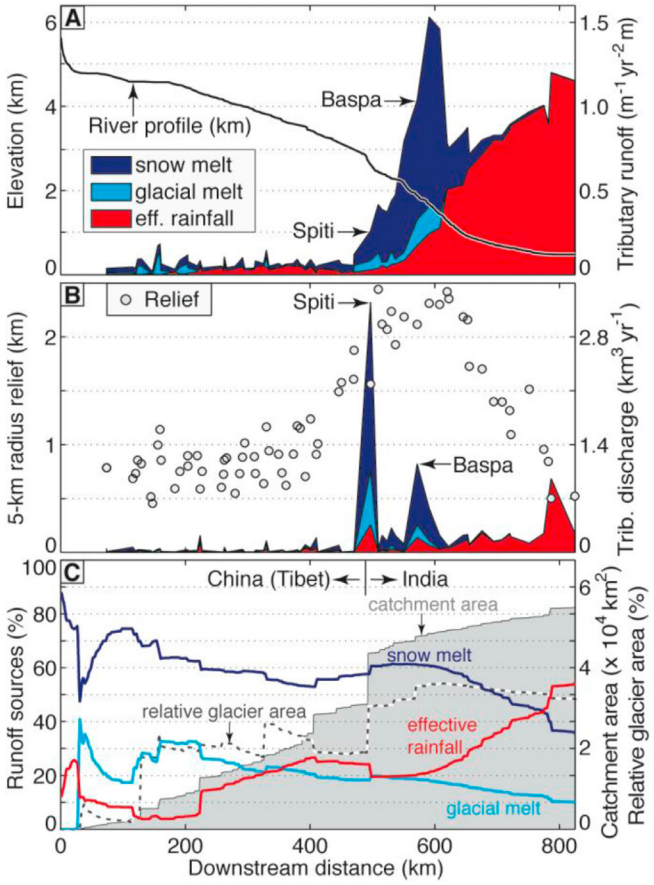

Fig. 13. (A) Distance and elevation of the Sutlej longitudinal river profile along with stacked mean annual (2000–2012) runoff of tributaries > 100 km^2. (B) 5-km radius local relief and mean annual (2000–2012) river discharge of Sutlej River tributaries > 100 km^2. Color-coding is given in (A). (C) Runoff sources of the mean annual Sutlej river discharge along its river profile. Grey area indicated the catchment area along the downstream distance with relative glacier area indicated by the dash line. (For interpretation of the references to color in this figure legend, the reader is referred to the web version of this article).

Annual river discharge throughout the Sutlej Valley is characterized by a pronounced seasonal cycle with low flow during winter and peak runoff during summer (Fig. 15). Snow melt initiates in March and dominates river discharge until June regardless of geographic location. During that period snow melt in the Sutlej Valley successively progresses to higher elevations, with peak snow melt at elevations of 4500 to 5500 m asl. From June to September monsoonal rainfall and glacier melt contribute approximately equal to river discharge at and upstream of the main Himalayan crest.

5.3. Annual variations of hydrological components

The observed Sutlej River discharge at the mountain front has a high annual variability, with discharge varying by almost a factor of two between individual years (i.e., 2004 and 2005/2010, Fig. 16D). Comparing the annual variation of ground-based measurements with simulated runoff of each hydrological component, we find that variations in snow melt ($r^2 = 0.69$) and re-calibrated TRMM-derived rainfall ($r^2 = 0.64$) are captured well (Fig. 16A and B). We also find an inverse correlation ($r^2 = 0.59$) between the observed winter snowfall, which is represented by snow melt (Fig. 16B), and the glacier melt during the subsequent summer (Fig. 16C). In other words, when winter snowfall is high, glacier melting during the following summer is low. The varying time spans of annual snow cover on glaciers and thus the variation in the glacier melt duration explains 86% of the annual variations in glacier melt. Thus, winter snowfall on glaciers contributes not only to glacial accumulation but also influences glacial ablation, as prolonged snow cover shields glaciers from radiative heating in the subsequent summer season [101]. The modeled annual variations in glacial ablation agree with ablation stake measurements of the nearby Chhota Shigri Glacier, which reveal significant decreases in glacier melt during 2005, 2009, and 2010 [5]. Our modeled mean specific ablation rates for the entire Sutlej catchment based on the glacier melt contribution to river discharge and the glacial surface area (1761 km^2) vary considerably between 2000 and 2012 with mean summer mass balance of -1.33 ± 0.35 m/yr.

Differences in temperature and precipitation in the western Himalaya were particularly high between 2004 and 2005. Low snow- and rainfall occurred in conjunction with high temperatures in 2004, whereas high snow- and rainfall accompanied low temperatures in 2005 (Fig. 17). As a result river discharge in 2004 was almost half the volume as of 2005. However, the low runoff from snow melt and rainfall in 2004 was extenuated by high glacier melt rates (17.3%), favored by high temperatures and a longer melting period due to low snow cover on glaciers (Fig. 17).

6. Discussion

6.1. Limits of the hydrological model

Due to the remoteness and climatic variability of the Sutlej Valley it is difficult to model its hydrology based on sparse ground-station coverage alone. Therefore, we based our hydrological model on calibrated remote-sensing data, which we validated with a unique ground-station dataset. Despite our use of remote-sensing data with high spatial and temporal resolution, several shortcomings of the input data and the model setup warrant attention when interpreting the results:

First, our modeling approach is deliberately simple to rule out unknown parameters that are difficult to constrain. We neglected refreezing of snow and ice melt, sublimation of snow and ice, losses to the groundwater system by deep seepage, turbulent energy exchange (e.g., rain on snow events), and transient water storage in soils and vegetation. The latter may be of lower importance in the upstream parts of our study area, because vegetation cover is only pertinent in the lower-elevation regions of the catchment area (Fig. S1). However, larger discrepancies between observed and modeled river discharge at the lowermost gauging station at Bhakra (Fig. 16D) potentially derive from lacking soil–water storage, especially during exceptionally warm and dry years with high soil infiltration rates as occurred in 2004. The effect of neglecting the aforementioned processes is difficult to estimate as relevant data on their implications on river discharge in the Himalaya is largely missing.

Second, there exists a trade-off in the TRMM 3B42 precipitation product between high temporal (3 h) but low spatial resolution (30 × 30 km^2). Consequently, TRMM 3B42 would not capture high-spatial variability of monsoonal rainfall that could result from small-scale convection, for example. However, the high sampling rate is crucial to detect the occurrence of convective monsoonal rainstorms that have short lifetimes of half an hour to several hours and small spatial footprints of a few to several dozen km^2 [10]. Overall, we find that in those areas where annual rainfall is generally high (> 0.7 m/yr), TRMM 3B42 performs reasonably well compared to the ground based measurements, whereas it performs poor in areas where annual rainfall is lower (<= 0.7 m/yr). However, because the contribution of rainfall as compared to snow and ice melt to river discharge is much lower in the latter areas, we still obtain reasonable model results.

Third, the air temperature data that drive the thermal snow and glacier melt module are based on MODIS LST data, which we scaled

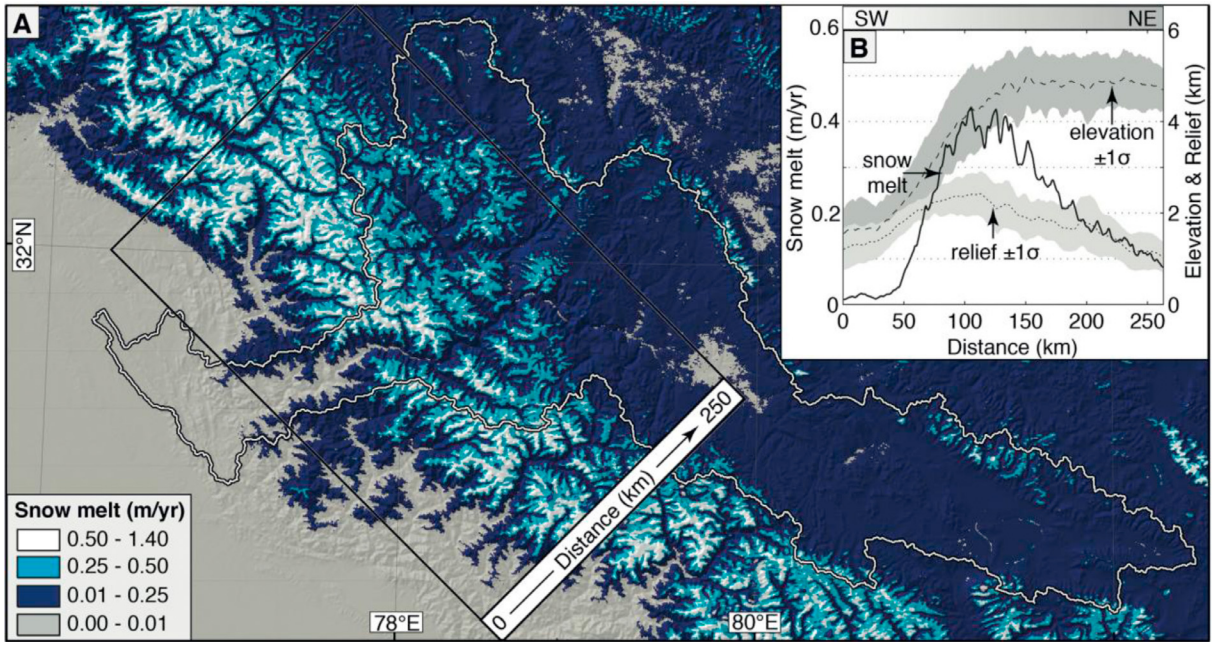

Fig. 14. (A) Mean annual snow melt (October 2001–September 2012) in the western Himalaya based on average snow melt factors of srf_s = 0.04 mm W^{-1} m^2 day^{-1} and tf_s = 2 mm $°C^{-1}$ day^{-1} (B) 270-km wide swath profile across the western Himalaya showing the average distribution of snow melt along with elevation (± 1σ) and a 5-km radius relief (± 1σ).

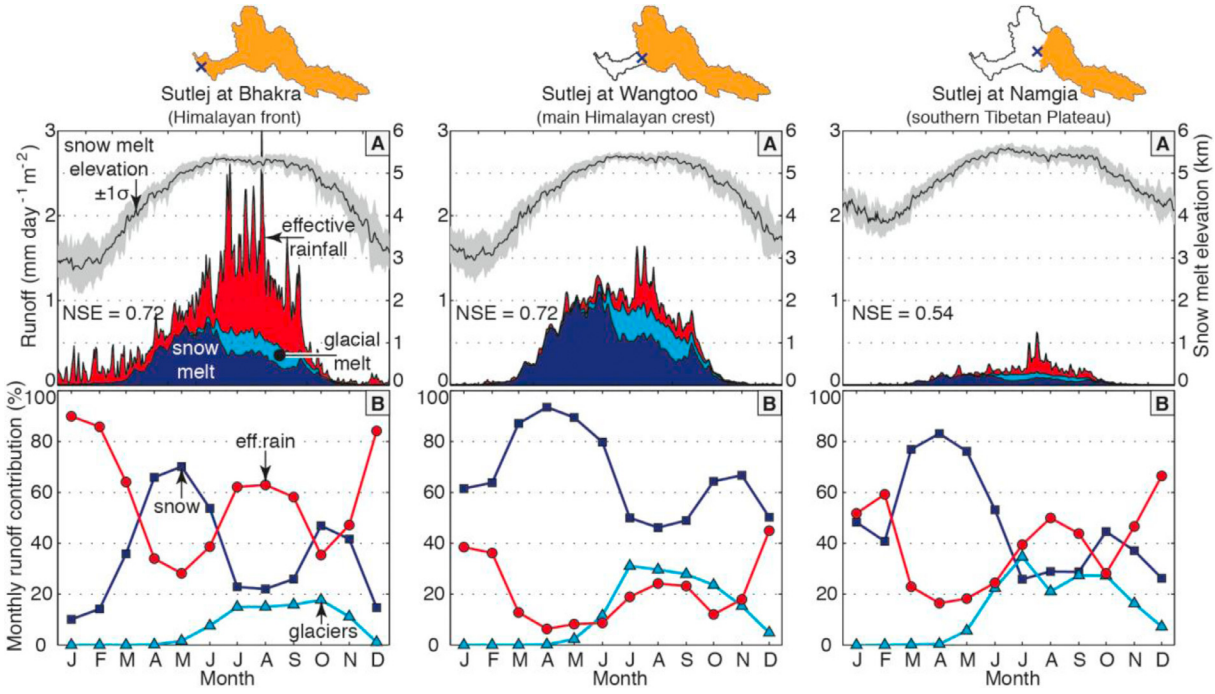

Fig. 15. (A) Mean daily runoff of stacked hydrologic components for the Sutlej River (2000–2012) at Bhakra, Wangtoo and Namgia gauging stations (cf. Fig. 1). Mean catchment-wide snow melt elevation (± 1σ) increases to above 5000 m asl during the summer months. (B) Mean monthly percentages to total runoff as shown in A.

by linear regressions with air temperature records from five weather stations. Despite the large altitudinal range of 2880 m among these stations, the relationship between air and surface temperatures may vary at higher elevations and in regions with contrasting land cover and radiation fluxes. This complexity may affect high-elevation low-relief region that experience high radiative heating during summer, but it presumably has a low impact on snow-covered areas and therefore snow melt.

Fourth, our shortwave-radiation and temperature factors for snow and ice melt (Eqs. (2) and (3)) are temporally constant but vary systematically between catchments as they decrease with increasing mean catchment elevation. These variations result from our model optimization process and might be related to the following causes: (1) sublimation of snow and ice increases with elevation, which reduces the energy available for melt and thus lowers the corresponding melt factors [59]; (2) losses to the groundwater system by deep seepage are likely to increase with increasing catchment areas at higher elevations; and (3) larger discrepancies between actual and modeled temperatures at higher elevations may similarly affect melt factors to compensate for increased melt rates.

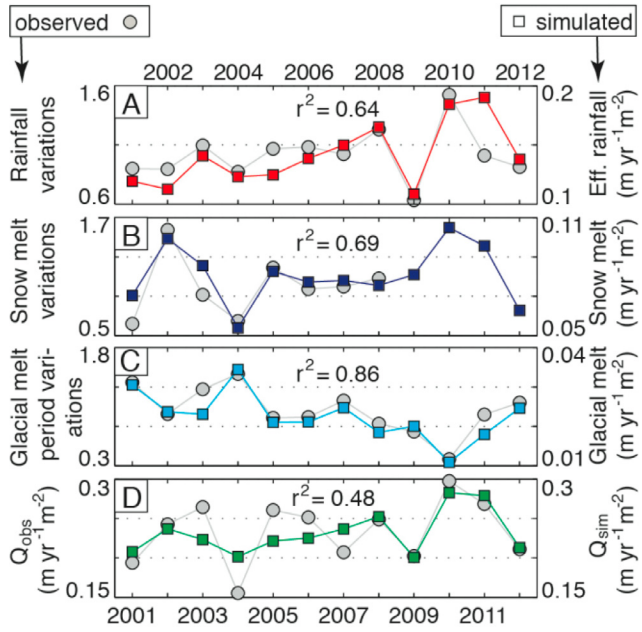

Fig. 16. Comparison of inter-annual variations in observed and simulated hydrological components within the Sutlej Valley. (A) Normalized mean annual rainfall records of 23 weather stations versus the modeled mean annual runoff from effective rainfall. (B) Normalized mean annual SWE records of 15 weather stations (2001–2008) versus the modeled mean annual snow melt runoff. (C) Normalized mean annual glacier melt period based on MODIS snow-cover data on glaciers versus modeled mean annual glacier melt runoff. (D) Observed river discharge versus modeled river discharge for the Sutlej River at Bhakra. The simulated runoff components in A, B, and C add up to the simulated river discharge in D.

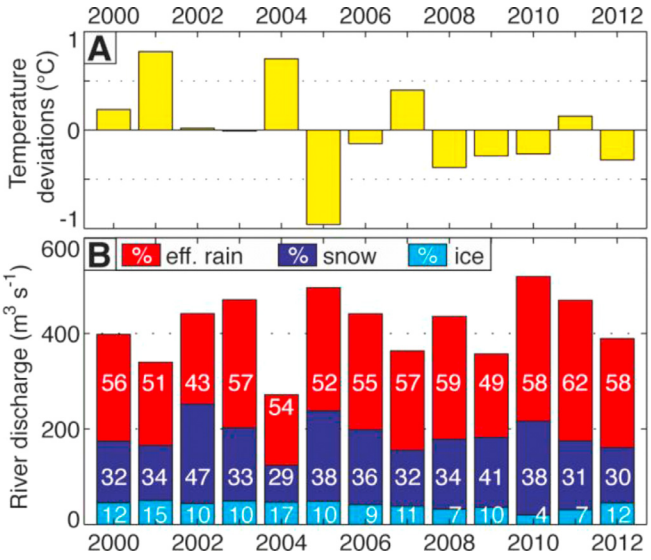

Fig. 17. (A) Mean annual temperature deviations in Kalpa (Fig. 1) from the average temperature of 10.44 °C between 2000 and 2012. (B) Observed mean annual river discharge divided in its runoff components effective rainfall, snow melt, and glacier melt based on the hydrological modeling results for the Sutlej River at Bhakra. White numbers indicate the relative runoff contribution to the annual river discharge in %.

6.2. Benefits and limits of remote sensing data in hydrological models

Based on our modeling results and previous studies on remote sensing products we aim to evaluate the benefits and limits of remote sensing data in hydrological modeling studies. In this study we used different remote sensing products that are based on different wavelengths of the electromagnetic spectrum ranging from (1) reflected solar radiation for snow, cloud, and glacial cover as well as evapotranspiration via (2) thermal infrared emissions for land surface temperature data to (3) reflected microwave radiation data for rainfall rate estimates. Remote sensing observations bear the potential to detect the spatial and temporal variability of hydrometeorological states (e.g. snow cover) and fluxes (e.g. rainfall rate) with an associated uncertainty [90]. These ambiguities derive from varying surface and atmospheric conditions, as well as specific sensor characteristics and data processing methods [28]. Consequently, remote sensing data need to be evaluated based on ground observations to verify their specific and general applicability in hydrologic models.

In general, satellite data can be highly beneficial in mountainous or remote regions with sparse ground observations and/or a high spatial variability in the state or flux of interest. In most instances the value of remote sensing data for hydrological models depends on its ability to detect the spatial and temporal variability of hydrometeorological states and fluxes. For example, glacier outlines are characterized by relatively low temporal variations and can be mapped accurately with sensors of high spatial resolution (e.g. Landsat) if challenges like debris, snow, and cloud cover can be addressed [35]. Similarly, moderate snow cover and albedo changes in space and time can be depicted accurately with sensors of high temporal resolution (e.g. MODIS, AVHRR) [47,76]. In contrast, convective monsoonal rainstorms have a relatively short lifetime, which makes it challenging to detect their magnitude and spatial distribution with repetitive snapshots from space (e.g. TRMM) [102]. Therefore, ground-based rainfall records are highly advantageous to calibrate remote sensing data on regional scales [46]. Overall, satellite-based precipitation products can significantly improve hydrologic investigations in areas with sparse weather station records [74]. Conversely, a dense network of rainfall records is likely to outperform satellite-based rainfall estimates, as indicated by the model performance comparison in the Baspa catchment (Table 5). Similarly, we estimated cloud-cover fraction based on two measurements per day (i.e. MODIS Aqua and Terra), which can be improved by including additional cloud-cover observations during the daytime. Another challenge for snow and glacier melt models is to accurately infer air temperatures in complex terrain [66]. We compared three approaches to compute air temperatures, which comprise: (1) seasonally constant lapse rate, (2) seasonally varying lapse rate, and (3) MODIS LST scaling. Among these different air temperature interpolation methods, we find the highest accuracies for the second and third approach. Presumably, a remote sensing based approach to infer air temperatures outperforms a varying lapse rate approach on regional scales (>10,000 km^2) with few weather stations, whereas the latter approach is likely to be more suitable on smaller scales (<1000 km^2) with multiple station records. In summary, it depends on the specific data availability if ground based, spaceborne, or combined observations are most suitable to map out the spatial and temporal variability of the state or flux of interest.

6.3. Comparison with previous studies

Previously, Bookhagen and Burbank [18] and Singh and Jain [96] modeled the hydrological budget of the Sutlej River using different approaches. Bookhagen and Burbank [18] modeled mean monthly river discharge, based on TRMM 2B31 data to derive rainfall quantities and MODIS data to model snowmelt and evapotranspiration. Their study indicates a snowmelt and rainfall contributions of 57% and 43%, respectively [18]. Singh and Jain [96] modeled daily Sutlej River discharge for six years between 1988 and 1999 based on isothets from ten rainfall stations to estimate rainfall quantities and snow cover data derived from Landsat MSS and IRS LISS-I data to model snow melt in different elevation zones. Their estimate of 68% snowmelt and 32% rainfall contributions to the Sutlej River discharge, on average, is constrained to the Indian part of the Sutlej River basin [96]. Considering the different modeling approaches, model input data, spatial and temporal scales, and target areas it is not

surprising that our results (55% effective rainfall, 35% snow melt, 10% glacier melt) deviate from the latter study.

Our estimate of average glacial ablation in the Sutlej catchment (1.33 ± 0.35 m/yr) and average range of snow accumulation (0–1.4 m/yr water equivalent) are well within range of glacier mass balances estimates of −0.15 to −0.75 m/yr in the region [5,14,56,105]. Immerzeel et al. [50] estimated similar precipitation magnitudes (1–2 m/yr) in regions > 4000 m asl in the Hunza catchment of the Karakorum based on glacier mass balance models. Moreover, we re-calibrated TRMM 3B42 rainfall estimates with measurement from more than 80 weather station, which further compare well with river discharge magnitudes (Table 5). In addition, our melt parameters are in general agreement with parameters used by Pellicciotti et al. [78], although a direct comparison of model parameters is generally hampered by a deviating modeling approaches and varying geographic or climatic influences.

7. Conclusion

In this study, we provide a comprehensive analysis of hydrologic components and their contribution to daily Sutlej River discharge, based on a simple hydrological model that uses calibrated remote-sensing data. Model performance was improved by (1) filling cloud cover gaps in the fractional snow cover data, as well as identifying cloud pixels misclassified as snow, and correcting for viewing angle artifacts, (2) scaling MODIS surface temperatures to observed air temperatures, (3) incorporating daily fractional cloud cover data in the net radiation balance, and by (4) calibrating rainfall estimates based on TRMM 3B42 data with data from 84 weather stations. Calibrating the rainfall data is particularly relevant in the Sutlej catchment as the TRMM 3B42 data moderately well depicts rainfall in humid frontal regions of the Himalaya within 6% mismatch of the mean monthly weather station records, but significantly overestimates weather station rainfall by a factor of 2–5 in the orogenic interior (elevations > 2000 m asl). This bias follows an inverse power–law relationship with mean annual precipitation and suggests that TRMM 3B42 performs poorly in semi-arid to arid regions of high relief and elevation.

Based on our modeling results, the average annual Sutlej River discharge at the mountain front (Sutlej River at Bhakra) is sourced to ~55% by effective rainfall, ~35% by snow melt, and ~10% by glacier melt. The discharge components vary strongly by season with snow melt dominating (63%) the pre-monsoon season (April–June) whereas the summer season from July to September is dominated by rainfall (61%), followed by snow (24%) and glacier melt (15%). Thus, transient water storage in ice and snow is an important source for discharge in the Sutlej River. Peak discharges and daily variations are usually controlled by rainfall events, which increases the importance of transiently stored water sources to continuous downstream water supply. This water storage is key for maintaining hydropower and agriculture in the downstream areas of the Sutlej River.

Snow and glacier melt contributions to discharge in the western Himalaya is highest near the main Himalayan crest, about 100 km inwards from the mountain front (Fig. 14). Downstream or windward of the main Himalayan crest, rainfall contribution becomes more important during both the winter and summer seasons. Pronounced inter-annual variations in winter snowfall also affect glacier melt, as the snow-cover duration controls radiation influx during the subsequent summer season. Based on our model, the average glacier melt in the Sutlej Valley between 2001 and 2012 has a water equivalent of 1.33 ± 0.35 m/yr, averaged over an ice-covered area of 1761 km^2. The importance of glacier melt to balance river discharge variability and to countervail low precipitation runoff was particularly noticeable during the exceptionally warm and dry year 2004. Under scenarios of future climate change, including higher temperatures, rising snowlines and declining glaciers, the decadal-time scale discharge of the Sutlej River is likely to become more variable and reduced, especially in the high-elevation internal parts of the orogen.

Acknowledgments

This research was funded by the German Science Foundation (DFG, GRK 1364) and carried out at Potsdam University and the GFZ German Research Centre for Geosciences. The data used in this study were acquired as part of the Tropical Rainfall Measuring Mission (TRMM) sponsored by the Japan National Space Development Agency (NASDA) and the NASA. Bodo Bookhagen was supported with Grants from NASA (NNX08AG05G) and NSF (EAR 0819874). We thank the employees of BBMB, HPSEB and JayPee Group, who generously shared their weather station and river discharge records with us. We also appreciate that Holger Frey provided his data on glacier outlines for us. We are grateful to Tashi Longpo, Swami Ray, and Bishan Lal for their enduring support during fieldwork. Ground station data used in this study (e.g. river discharge, precipitation) can be provided upon request to the corresponding author. We thank Editor P. D'Odorico and reviewers J. Dozier, M. Engelhardt, and F. Pellicciotti for their constructive reviews and thoughtful comments.

Supplementary materials

Supplementary material associated with this article can be found, in the online version, at doi:10.1016/j.advwatres.2015.12.004.

References

[1] Akhtar M, Ahmad N, Booij MJ. The impact of climate change on the water resources of Hindukush–Karakorum–Himalaya region under different glacier coverage scenarios. J Hydrol 2008;355(1-4):148–63. http://dx.doi.org/10.1016/j.jhydrol.2008.03.015.
[2] Alford D, Armstrong R. The role of glaciers in stream flow from the Nepal Himalaya. Cryosphere 2010;4(2):469–94. http://dx.doi.org/10.5194/tcd-4-469-2010.
[3] Allen PM, Arnold JC, Byars BW. Downstream channel geometry for use in planning level models. J Am Water Resour Assoc 1994;30(4):663–71. http://dx.doi.org/10.1111/j.1752-1688.1994.tb03321.x.
[4] Anderson, E.A. (1976), A point energy and mass balance model for a snow cover, NOAA Technical Report, vol. 19, 150 pp, NOAA.
[5] Azam MF, et al. From balance to imbalance: a shift in the dynamic behaviour of Chhota Shigri glacier, western Himalaya, India. J Glaciol 2012;58(208):315–24. http://dx.doi.org/10.3189/2012JoG11J123.
[6] Bales RC, Molotch NP, Painter TH, Dettinger MD, Rice R, Dozier J. Mountain hydrology of the western United States. Water Resour Res 2006;42(8):1–13. http://dx.doi.org/10.1029/2005WR004387.
[7] Barnett TP, Adam JC, Lettenmaier DP. Potential impacts of a warming climate on water availability in snow-dominated regions. Nature 2005;438(7066):303–9. http://dx.doi.org/10.1038/nature04141.
[8] Barros AP, Lang TJ. Monitoring the monsoon in the Himalayas: observations in Central Nepal, June 2001. Mon Weather Rev 2003;131(7):1408–27. http://dx.doi.org/10.1175/1520-0493(2003)131⟨1408:MTMITH⟩2.0.CO;2.
[9] Barros AP, Kim G, Williams E, Nesbitt SW. Probing orographic controls in the Himalayas during the monsoon using satellite imagery. Nat Hazards Earth Syst Sci 2004;4(1):29–51. http://dx.doi.org/10.5194/nhess-4-29-2004.
[10] Barros AP, Chiao S, Lang TJ, Burbank D, Putkonen J. From weather to climate – seasonal and interannual variability of storms and implications for erosion processes in the Himalaya. Tectonics, Climate, and Landscape Evolution 2006;398:17–38 Special Paper 398. http://dx.doi.org/10.1130/2006.2398(02).
[11] Barry RG, Chorley RJ. Atmosphere, weather, and climate. London: Routledge; 2003. p. 421.
[12] Bergström S. Development and application of a conceptual runoff model for Scandinavian catchments. Norrköping: Swedish Meteorological and Hydrological Institute (SMHI); 1976.
[13] Bergström, S. (1992), *The HBV model – its structure and applications*, 35 pp, Swedish Meteorological and Hydrological Institute (SMHI), Norrköping.
[14] Berthier E, Arnaud Y, Kumar R, Ahmad S, Wagnon P, Chevallier P. Remote sensing estimates of glacier mass balances in the Himachal Pradesh (Western Himalaya, India). Remote Sens Environ 2007;108(3):327–38. http://dx.doi.org/10.1016/j.rse.2006.11.017.
[15] Bhambri R, Bolch T. Glacier mapping: a review with special reference to the Indian Himalayas. Prog Phys Geogr 2009;33(5):672–704. http://dx.doi.org/10.1177/0309133309348112.
[16] Böhner J, Antonic O. Chapter 8 land-surface parameters specific to topo-climatology. In: Hengl T, Reuter HI, editors. Developments in soil science. Elsevier; 2009. p. 195–226.

[17] Bookhagen B, Burbank DW. Topography, relief, and TRMM-derived rainfall variations along the Himalaya. Geophys Res Lett 2006;33(8):L08405. http://dx.doi.org/10.1029/2006GL026037.

[18] Bookhagen B, Burbank DW. Toward a complete Himalayan hydrological budget: spatiotemporal distribution of snowmelt and rainfall and their impact on river discharge. J Geophys Res 2010;115:F03019. http://dx.doi.org/10.1029/2009JF001426.

[19] Bookhagen B, Thiede RC, Strecker MR. Abnormal monsoon years and their control on erosion and sediment flux in the high, arid northwest Himalaya. Earth Planet Sci Lett 2005;231(1-2):131–46. http://dx.doi.org/10.1016/j.epsl.2004.11.014.

[20] Braun LN, Grabs W, Rana B. Application of a conceptual precipitation runoff model in the Langtang Khola basin, Nepal Himalaya. In: Young G, editor. Snow and Glacier Hydrology. IAHS Publ. 218. Wallingford, UK: IAHS Press; 1993. p. 221–37.

[21] Brock BW, Mihalcea C, Kirkbride MP, Diolaiuti G, Cutler MEJ, Smiraglia C. Meteorology and surface energy fluxes in the 2005–2007 ablation seasons at the Miage debris-covered glacier, Mont Blanc Massif, Italian Alps. J Geophys Res 2010;115(D9):1–16. http://dx.doi.org/10.1029/2009JD013224.

[22] Brubaker K, Rango A, Kustas W. Incorporating radiation inputs into the snowmelt runoff model. Hydrol Process 1996;10(10):1329–43. http://dx.doi.org/10.1002/(SICI)1099-1085(199610)10:10⟨1329::AID-HYP464⟩3.0.CO;2-W.

[23] Cleugh H, Leuning R, Mu Q, Running S. Regional evaporation estimates from flux tower and MODIS satellite data. Remote Sens Environ 2007;106(3):285–304. http://dx.doi.org/10.1016/j.rse.2006.07.007.

[24] Coll C, Caselles V, Galve J, Valor E, Niclos R, Sanchez J, Rivas R. Ground measurements for the validation of land surface temperatures derived from AATSR and MODIS data. Remote Sens Environ 2005;97(3):288–300. http://dx.doi.org/10.1016/j.rse.2005.05.007.

[25] Craddock WH, Burbank DW, Bookhagen B, Gabet EJ. Bedrock channel geometry along an orographic rainfall gradient in the upper Marsyandi River valley in central Nepal. J Geophys Res-Earth Surf 2007;112:17. http://dx.doi.org/10.1029/2006JF000589.

[26] Dinku T, Chidzambwa S, Ceccato P, Connor SJ, Ropelewski CF. Validation of high-resolution satellite rainfall products over complex terrain. Int J Remote Sens 2008;29(14):4097–110. http://dx.doi.org/10.1080/01431160701772526.

[27] Dozier J, Warren SG. Effect of viewing angle on the infrared brightness temperature of snow. Water Resour Res 1982;18(5):1424–34. http://dx.doi.org/10.1029/WR018i005p01424.

[28] Dozier J, Painter TH, Rittger K, Frew JE. Time-space continuity of daily maps of fractional snow cover and albedo from MODIS. Adv Wat Resour 2008;31(11):1515–26. http://dx.doi.org/10.1016/J.Advwatres.2008.08.011.

[29] Dury GH. An introduction to environmental systems. New Hampshire: Heinemann, Exeter; 1981.

[30] Einfalt T, Michaelides S. Quality control of precipitation data. In: Michaelides S, editor. Precipitation: advances in measurement, estimation and prediction. Berlin, Heidelberg: Springer; 2008. p. 101–26.

[31] FAO. Land cover map of Himalaya region, Rome: Food and agriculture organization of the United Nations (FAO); 2009. edited.

[32] Farr TG, et al. The shuttle radar topography mission. Rev Geophys 2007;45(2):1–33. http://dx.doi.org/10.1029/2005RG000183.

[33] Fisher GB, Bookhagen B, Amos CB. Channel planform geometry and slopes from freely available high-spatial resolution imagery and DEM fusion: Implications for channel width scalings, erosion proxies, and fluvial signatures in tectonically active landscapes. Geomorphology 2013;194:46–56. http://dx.doi.org/10.1016/j.geomorph.2013.04.011.

[34] Franz KJ, Butcher P, Ajami NK. Addressing snow model uncertainty for hydrologic prediction. Adv Water Resour 2010;33(8):820–32. http://dx.doi.org/10.1016/j.advwatres.2010.05.004.

[35] Frey H, Paul F, Strozzi T. Compilation of a glacier inventory for the western Himalayas from satellite data: methods, challenges, and results. Remote Sens Environ 2012;124:832–43. http://dx.doi.org/10.1016/j.rse.2012.06.020.

[36] Fritsch FN, Carlson RE. Monotone piecewise cubic interpolation. SIAM J Numer Anal 1980;7(2):238–46. http://dx.doi.org/10.1137/0717021.

[37] Gafurov A, Bárdossy A. Cloud removal methodology from MODIS snow cover product. Hydrol Earth Syst Sci 2009;13(7):1361–73. http://dx.doi.org/10.5194/hess-13-1361-2009.

[38] Gurtz J, Baltensweiler A, Lang H. Spatially distributed hydrotope-based modelling of evapotranspiration and runoff in mountainous basins. Hydrol Process 1999;13(17):2751–68. http://dx.doi.org/10.1002/(SICI)1099-1085(19991215)13:17⟨2751::AID-HYP897⟩3.0.CO;2-O.

[39] Hall DK, Riggs GA. Accuracy assessment of the MODIS snow products. Hydrol Process 2007;21(12):1534–47. http://dx.doi.org/10.1002/hyp.6715.

[40] Hall DK, Riggs GA, Salomonson VV. Development of methods for mapping global snow cover using moderate resolution imaging spectroradiometer data. Remote Sens Environ 1995;54(2):127–40. http://dx.doi.org/10.1016/0034-4257(95)00137-P.

[41] Hall DK, Riggs GA, Salomonson VV, DiGirolamo NE, Bayr KJ. MODIS snow-cover products. Remote Sens Environ 2002;83(1-2):181–94. http://dx.doi.org/10.1016/S0034-4257(02)00095-0.

[42] He ZH, Parajka J, Tian FQ, Blöschl G. Estimating degree-day factors from MODIS for snowmelt runoff modeling. Hydrol Earth Syst Sci 2014;18(12):4773–89. http://dx.doi.org/10.5194/hess-18-4773-2014.

[43] Hobley DEJ, Sinclair HD, Mudd SM. Reconstruction of a major strom event from its geomorphic signature: the Ladakh cloudburst. Geology 2012;40(6):483–6 6 August 2010.. http://dx.doi.org/10.1130/G32935.1.

[44] Hock R. A distributed temperature-index ice- and snowmelt model including potential direct solar radiation. J Glaciol 1999;45(149):101–11.

[45] Hock R. Temperature index melt modelling in mountain areas. J Hydrol 2003;282(1-4):104–15. http://dx.doi.org/10.1016/S0022-1694(03)00257-9.

[46] Huffman GJ, Adler RF, Bolvin DT, Gu G, Nelkin EJ, Bowman KP, Hong Y, Stocker EF, Wolff DB. The TRMM Multisatellite Precipitation Analysis (TMPA): quasi-global, multiyear, combined-sensor precipitation estimates at fine scales. J Hydrom 2007;8(1) pp. 38–38 http://dx.doi.org/10.1175/JHM560.1 .

[47] Hüsler F, Jonas T, Wunderle S, Albrecht S. Validation of a modified snow cover retrieval algorithm from historical 1-km AVHRR data over the European Alps. Remote Sens Environ 2012;121(0):497–515. http://dx.doi.org/10.1016/j.rse.2012.02.018.

[48] Huss M, Farinotti D, Bauder A, Funk M. Modelling runoff from highly glacierized alpine drainage basins in a changing climate. Hydrol Process 2008;22(19):3888–902. http://dx.doi.org/10.1002/hyp.7055.

[49] Immerzeel W, van Beek LPH, Bierkens MFP. Climate change will affect the Asian water towers. Science 2010;328(5984):1382–5. http://dx.doi.org/10.1126/science.1183188.

[50] Immerzeel W, Pellicciotti F, Shrestha AB. Glaciers as a proxy to quantify the spatial distribution of precipitation in the Hunza Basin. Mt. Res Dev 2012;32(1):30–8. http://dx.doi.org/10.1659/mrd-journal-d-11-00097.1.

[51] Immerzeel W, Droogers P, Dejong S, Bierkens M. Large-scale monitoring of snow cover and runoff simulation in Himalayan river basins using remote sensing. Remote Sens Environ 2009;113(1):40–9. http://dx.doi.org/10.1016/j.rse.2008.08.010.

[52] IPCC. In: Field CB, Barros VR, Dokken DJ, Mach KJ, Mastrandrea MD, Bilir TE, Chatterjee M, Ebi KL, Estrada YO, Genova RC, Girma B, Kissel ES, Levy AN, MacCracken S, Mastrandrea PR, White LL, editors. Climate change 2014: impacts, adaptation, and vulnerability. Part A: global and sectoral aspects. contribution of working group II to the fifth assessment report of the intergovernmental panel on climate change. Cambridge, United Kingdom and New York, NY, USA: Cambridge University Press; 2014. p. 1132.

[53] Jeelani G, Feddema JJ, van der Veen CJ, Stearns L. Role of snow and glacier melt in controlling river hydrology in Liddar watershed (western Himalaya) under current and future climate. Water Resour Res 2012;48(12):W12508. http://dx.doi.org/10.1029/2011wr011590.

[54] Jin J, Gao X, Sorooshian S, Yang Z-L, Bales R, Dickinson RE, Sun S-F, Wu G-X. One-dimensional snow water and energy balance model for vegetated surfaces. Hydrol Process 1999;13(14-15):2467–82. http://dx.doi.org/10.1002/(sici)1099-1085(199910)13:14/15⟨2467::aid-hyp861⟩3.0.co;2-j.

[55] Jolliffe IT, Stephenson DB. Forecast verification: a practitioner's guide in atmospheric science. Hoboken, NJ: Wiley; 2003. p. 240.

[56] Kääb A, Berthier E, Nuth C, Gardelle J, Arnaud Y. Contrasting patterns of early twenty-first-century glacier mass change in the Himalayas. Nature 2012;488(7412):495–8. http://dx.doi.org/10.1038/nature11324.

[57] Klein AG, Barnett AC. Validation of daily MODIS snow cover maps of the Upper Rio Grande River Basin for the 2000–2001 snow year. Remote Sens Environ 2003;86(2):162–76. http://dx.doi.org/10.1016/S0034-4257(03)00097-X.

[58] Kumar M, Marks D, Dozier J, Reba M, Winstral A. Evaluation of distributed hydrologic impacts of temperature-index and energy-based snow models. Adv Water Resour 2013;56(0):77–89 http://dx.doi.org/10.1016/j.advwatres.2013.03.006 .

[59] Lang H, Braun L. On the information content of air temperature in the context of snow melt estimation. In: Molar L, editor. Hydrology of mountainous areas. Zürich: IAHS; 1990. p. 347–54.

[60] Leopold L, Maddock T. The hydraulic geometry of stream channels and some physiographic implications. United States Geological Survey; 1953. Professional Paper 252.

[61] Li X, Williams MW. Snowmelt runoff modelling in an arid mountain watershed, Tarim Basin, China. Hydrol Process 2008;22(19):3931–40. http://dx.doi.org/10.1002/hyp.7098.

[62] Lundquist JD, Cayan DR. Surface temperature patterns in complex terrain: daily variations and long-term change in the central Sierra Nevada, California. J Geophys Res 2007;112(D11):1–15. http://dx.doi.org/10.1029/2006JD007561.

[63] Martinec J. Snowmelt – runoff model for stream flow forecasts. Nord Hydrol 1975;6(3):145–54. http://dx.doi.org/10.2166/nh.1975.010.

[64] Mattson LE, Gardner JS, Young GJ. Ablation on debris covered glaciers: an example from the Rakhiot Glacier, Punjab, Himalaya. In: Young GJ, editor. Proceedings international symposium on snow and glacier hydrology. Kathmandu: International Association of Hydrological Sciences. IAHS/AISH Publication; 1993. p. 289–96.

[65] Maussion F, Scherer D, Finkelnburg R, Richters J, Yang W, Yao T. WRF simulation of a precipitation event over the Tibetan Plateau, China – an assessment using remote sensing and ground observations. Hydrol Earth Syst Sci 2011;15(6):1795–817. http://dx.doi.org/10.5194/hess-15-1795-2011.

[66] Minder JR, Mote PW, Lundquist JD. Surface temperature lapse rates over complex terrain: lessons from the Cascade Mountains. J Geophys Res 2010;115(D14122):14113. http://dx.doi.org/10.1029/2009JD013493.

[67] Molotch NP, Norte D. Reconstructing snow water equivalent in the Rio Grande headwaters using remotely sensed snow cover data and a spatially distributed snowmelt model. Hydrol Process 2009;1089:1076–89. http://dx.doi.org/10.1002/hyp.7206.

[68] Monteith JL. Evaporation and environment. In: Proceedings of symposia on the society for experimental biology; 1965. p. 205–34.

[69] Mu Q, Zhao M, Running SW. Improvements to a MODIS global terrestrial evapotranspiration algorithm. Remote Sens Environ 2011;115(8):1781–800. http://dx.doi.org/10.1016/j.rse.2011.02.019.

[70] Mu Q, Heinsch FA, Zhao M, Running SW. Development of a global evapotranspiration algorithm based on MODIS and global meteorology data. Remote Sens Environ 2007;111(4):519–36. http://dx.doi.org/10.1016/J.Rse.2007.04.015.
[71] Mu Q, Jones LA, Kimball JS, McDonald KC, Running SW. Satellite assessment of land surface evapotranspiration for the pan-Arctic domain. Water Resour Res 2009;45(9):W09420. http://dx.doi.org/10.1029/2008wr007189.
[72] Nash JE, Sutcliffe JV. River flow forecasting through conceptual models. Part I: a discussion of principles. J Hydrol 1970;10:282–90. http://dx.doi.org/10.1016/0022-1694(70)90255-6.
[73] Ohmura A. Physical basis for the temperature-based melt-index method. J Appl Meteorol 2001;40(4):753–61. http://dx.doi.org/10.1175/1520-0450(2001)040%3C0753:PBFTTB%3E2.0.CO;2.
[74] Pan M, Li H, Wood E. Assessing the skill of satellite-based precipitation estimates in hydrologic applications. Water Resour Res 2010;46(9):1–10. http://dx.doi.org/10.1029/2009WR008290.
[75] Pandit MK, Bisht MS, Bhatt JP, Pattanayak SK, Nautiyal DC, Mehta R. Environmental impact assessment of luhri hydroelectric project, Himachal Pradesh. Delhi: Centre for inter-disciplinary studies of mountain & hill environment; 2010.
[76] Parajka J, Blöschl G. Validation of MODIS snow cover images over Austria. Hydrol Earth Syst Sci Discuss 2006;3(4):1569–601. http://dx.doi.org/10.5194/hess-10-679-2006.
[77] Pellicciotti F, Raschle T, Huerlimann T, Carenzo M, Burlando P. Transmission of solar radiation through clouds on melting glaciers: a comparison of parameterizations and their impact on melt modelling. J Glaciol 2011;57(202):367–81. http://dx.doi.org/10.3189/002214311796406013.
[78] Pellicciotti F, Brock B, Strasser U, Burlando P, Funk M, Corripio J. An enhanced temperature-index glacier melt model including the shortwave radiation balance: development and testing for Haut Glacier d'Arolla, Switzerland. J Glaciol 2005;51(175):573–87. http://dx.doi.org/10.3189/172756505781829124.
[79] Preparata FR, Shamos MI. Computational geometry: an introduction. New York: Springer-Verlag; 1985.
[80] Prince SD, Goetz SJ, Dubayah RO, Czajkowski KP, Thawley M. Inference of surface and air temperature, atmospheric precipitable water and vapor pressure deficit using advanced very high-resolution radiometer satellite observations: comparison with field observations. J Hydrol 1998;213(1-4):230–49. http://dx.doi.org/10.1016/S0022-1694(98)00210-8.
[81] Racoviteanu AE, Armstrong R, Williams MW. Evaluation of an ice ablation model to estimate the contribution of melting glacier ice to annual discharge in the Nepalese Himalaya. Water Resour Res 2013;49:5117–33. http://dx.doi.org/10.1002/wrcr.20370.
[82] Ragettli S, Pellicciotti F, Bordoy R, Immerzeel WW. Sources of uncertainty in modeling the glacio-hydrological response of a Karakoram watershed to climate change. Water Resour Res 2013;49:6048–66. http://dx.doi.org/10.1002/wrcr.20450.
[83] Rango A, Martinec J. Revisiting the degree-day method for snowmelt computations. Water Resour Bull 1995;31(4):657–69. http://dx.doi.org/10.1111/j.1752-1688.1995.tb03392.x.
[84] Reid TD, Brock BW. An energy-balance model for debris-covered glaciers including heat conduction through the debris layer. J Glaciol 2010;56(199):903–16. http://dx.doi.org/10.3189/002214310794457218.
[85] Rittger K, Painter TH, Dozier J. Assessment of methods for mapping snow cover from MODIS. Adv Water Resour 2013;51:367–80. http://dx.doi.org/10.1016/j.advwatres.2012.03.002.
[86] Rodell M, Velicogna I, Famiglietti JS. Satellite-based estimates of groundwater depletion in India. Nature 2009;460(7258):999–1002. http://dx.doi.org/10.1038/nature08238.
[87] Salomonson V, Apple. Estimating fractional snow cover from MODIS using the normalized difference snow index. Remote Sens Environ 2004;89(3):351–60. http://dx.doi.org/10.1016/j.rse.2003.10.016.
[88] Sapiano MRP. An evaluation of high resolution precipitation products at low resolution. Int J Climatol 2009;30(9):1416–22. http://dx.doi.org/10.1002/joc.1961.
[89] Scherler D, Bookhagen B, Strecker MR. Spatially variable response of Himalayan glaciers to climate change affected by debris cover. Nat Geosci 2011;4:156–9. http://dx.doi.org/10.1038/ngeo1068.
[90] Schmugge TJ, Kustas WP, Ritchie JC, Jackson TJ, Rango A. Remote sensing in hydrology. Adv Water Resour 2002;25(8-12):1367–85. http://dx.doi.org/10.1016/S0309-1708(02)00065-9.
[91] Schulze K, Hunger M, Döll P. Simulating river flow velocity on global scale. Adv Geosci 2005;5:133–6. http://dx.doi.org/10.5194/adgeo-5-133-2005.
[92] Schwanghart W, Scherler D. Short Communication: topoToolbox 2 – MATLAB-based software for topographic analysis and modeling in Earth surface sciences. Earth Surf Dyn 2014;2(1):1–7. http://dx.doi.org/10.5194/esurf-2-1-2014.
[93] Schwarze R, Droege W, Opherden K. Regional analysis and modelling of groundwater runoff components from catchments in hard rock areas. In: Diekkrüger B, Kirkby MJ, Schröder U, editors. Regionalisation in hydrology. Wallingford, UK: IAHS Press; 1999. p. 221–32.
[94] Singh P, Kumar N. Effect of orography on precipitation in the western Himalayan region. J Hydrol 1997;199(1-2):183–206. http://dx.doi.org/10.1016/S0022-1694(96)03222-2.
[95] Singh P, Jain SK. Snow and glacier melt in the Satluj River at Bhakra Dam in the western Himalayan region. Hydrol Sci J 2002;47(1):93–106. http://dx.doi.org/10.1080/02626660209492910.
[96] Singh P, Jain SK. Modelling of streamflow and its components for a large Himalayan basin with predominant snowmelt yields. Hydrol Sci J 2003;48(2):257–76. http://dx.doi.org/10.1623/hysj.48.2.257.44693.
[97] Singh P, Bengtsson L. Effect of warmer climate on the depletion of snowcovered area in the Satluj basin in the western Himalayan region. Hydrol Sci J 2003;48(3):413–25. http://dx.doi.org/10.1623/hysj.48.3.413.45280.
[98] Sorg A, Bolch T, Stoffel M, Solomina O, Beniston M. Climate change impacts on glaciers and runoff in Tien Shan (Central Asia). Nat Clim Change 2012;2(10):725–31. http://dx.doi.org/10.1038/nclimate1592.
[99] Stephens GL, Cess RD, Zhang MH, Pilewskie P, Valero FPJ. How much solar radiation do clouds absorb? Science 1996;271(5252):1131. http://dx.doi.org/10.1126/science.271.5252.1131.
[100] Swets JA. Form of empirical ROCs in discrimination and diagnostic tasks: implications for theory and measurement of performance. Psychol Bull 1986;99(2):181–98. http://dx.doi.org/10.1037/0033-2909.99.2.181.
[101] Thayyen RJ, Gergan JT, Dobhal DP. Role of glaciers and snow cover on headwater river hydrology in monsoon regime – micro-scale study of Din Gad catchment, Garhwal Himalaya, India. Curr Sci 2007;92(3):376–82.
[102] Tian YD, Peters-Lidard CD, Eylander JB, Joyce RJ, Huffman GJ, Adler RF, Hsu KL, Turk FJ, Garcia M, Zeng J. Component analysis of errors in satellite-based precipitation estimates. J Geophys Res 2009;114 pp. D24101.24101-24115. http://dx.doi.org/10.1029/2009jd011949.
[103] Viviroli D, Gurtz J, Zappa M. The Hydrological modelling system PREVAH. Geographica bernensia. Berne: Institute of Geography, University of Berne; 2007.
[104] Viviroli D, Zappa M, Gurtz J, Weingartner R. An introduction to the hydrological modelling system PREVAH and its pre- and post-processing-tools. Environ Model Softw 2009;24(10):1209–22. http://dx.doi.org/10.1016/J.Envsoft.2009.04.001.
[105] Wagnon P, et al. Four years of mass balance on Chhota Shigri Glacier, Himachal Pradesh, India, a new benchmark glacier in the western Himalaya. J Glaciol 2007;53(183):603–11. http://dx.doi.org/10.3189/002214307784409306.
[106] Wan Z. New refinements and validation of the MODIS land-surface temperature/emissivity products. Remote Sens Environ 2008;112(1):59–74. http://dx.doi.org/10.1016/j.rse.2006.06.026.
[107] Wan Z, Dozier J. A generalized split-window algorithm for retrieving land-surface temperature from space. IEEE Trans Geosci Remote Sens 1996;34(4):892–905. http://dx.doi.org/10.1109/36.508406.
[108] Wan Z, Zhang Y, Zhang Q. Quality assessment and validation of the MODIS global land surface temperature. Int J Remote Sens 2004;25(1):261–74. http://dx.doi.org/10.1080/0143116031000116417.
[109] WDI. World Bank, World development indicators. Manchester: University of Manchester; 2010.
[110] Winiger M, Gumpert M, Yamout H. Karakorum–Hindukush–western Himalaya: assessing high-altitude water resources. Hydrol Process 2005;19(12):2329–38. http://dx.doi.org/10.1002/hyp.5887.
[111] Wulf H, Bookhagen B, Scherler D. Seasonal precipitation gradients and their impact on fluvial sediment flux in the Northwest Himalaya. Geomorphology 2010;118(1-2):13–21. http://dx.doi.org/10.1016/J.Geomorph.2009.12.003.
[112] Wulf H, Bookhagen B, Scherler D. Climatic and geologic controls on suspended sediment flux in the Sutlej River Valley, western Himalaya. Hydrol Earth Syst Sci 2012;16(7):2193–217. http://dx.doi.org/10.5194/hess-16-2193-2012.
[113] Zhang L, Su F, Yang D, Hao Z, Tong K. Discharge regime and simulation for the upstream of major rivers over Tibetan Plateau. J Geophys Res: Atmos 2013. http://dx.doi.org/10.1002/jgrd.50665.